

**Baroclinic and barotropic annular variability in the
Northern Hemisphere**

David W. J. Thompson¹ and Ying Li

Department of Atmospheric Science, Colorado State University
Fort Collins, CO. USA

Submitted to Journal of Atmospheric Sciences

April 2014

Revised

August 2014

¹ Corresponding author address: David W. J. Thompson, Dept. of Atmospheric Science,
Colorado State University, Ft. Collins, CO. USA 80523.
E-mail: davet@atmos.colostate.edu

1 **Abstract**

2 Large-scale variability in the Northern Hemisphere (NH) circulation can be
3 viewed in the context of three primary types of structures: 1) teleconnection patterns; 2)
4 a barotropic annular mode; and 3) a baroclinic annular mode. The barotropic annular
5 mode corresponds to the northern annular mode (NAM) and has been examined
6 extensively in previous research. Here we examine the spatial structure and time
7 dependent behavior of the NH baroclinic annular mode (NBAM).

8 The NAM and NBAM have very different signatures in large-scale NH climate
9 variability. The NAM emerges as the leading principal component (PC) time series of the
10 *zonal-mean* kinetic energy. It dominates the variance in the wave fluxes of momentum,
11 projects weakly onto the eddy kinetic energy and wave fluxes of heat, and can be
12 modeled as Gaussian red noise with a timescale of ~10 days. In contrast, the NBAM
13 emerges as the leading PC time series of the *eddy* kinetic energy. It is most clearly
14 identified when the planetary-scale waves are filtered from the data, dominates the
15 variance in the synoptic-scale eddy kinetic energy and wave fluxes of heat, and has a
16 relatively weak signature in the zonal-mean kinetic energy and the wave fluxes of
17 momentum. The NBAM is marked by enhanced spectral power on timescales of ~20-25
18 days.

19 The NBAM is remarkably similar to its Southern Hemisphere counterpart despite
20 the pronounced interhemispheric differences in orography and land/sea contrasts.

21

22 **1. Introduction**

23 Large scale variability in the extratropical circulation is often examined in the
24 context of two primary classes of structures: “teleconnection patterns” and “annular
25 modes”.

26 Teleconnection patterns are typically defined on the basis of significant negative
27 correlations between widely separated points in the geopotential height field (e.g.,
28 Wallace and Gutzler 1981). They are generally regional in scale and thus project most
29 strongly onto climate variability over specific sectors of the hemisphere. In contrast, the
30 Northern and Southern annular modes (the NAM and SAM) are typically defined as the
31 leading empirical orthogonal functions of the hemispheric-scale geopotential height
32 and/or zonal wind fields (e.g., Kidson 1988; Hartmann and Lo 1998; Thompson and
33 Wallace 2000). In contrast to most teleconnection patterns, they are hemispheric in
34 scale and thus project onto climate variability throughout the extratropics of their
35 respective hemispheres.

36 Teleconnection patterns are frequently viewed in the context of their zonally
37 *asymmetric* components. The Pacific-North America pattern is dominated by wavelike
38 anomalies in the geopotential height field that stretch along a great circle route from the
39 central north Pacific to eastern North America (Wallace and Gutzler 1981; Quadrelli and
40 Wallace 2004); the North Atlantic Oscillation is characterized by north-south
41 fluctuations in the geopotential height field that have largest amplitude in the North
42 Atlantic sector (e.g., Wallace and Gutzler 1981; Hurrell 1995). In contrast, the NAM and
43 SAM are commonly viewed in the context of their zonally *symmetric* components. Both
44 are characterized by barotropic fluctuations in the extratropical circulation that exhibit a
45 high degree of longitudinal symmetry. The North Atlantic Oscillation teleconnection

46 pattern also has a pronounced zonally symmetric component and may be viewed as a
47 regional expression of the NAM (Wallace 2000).

48 In recent work (Thompson and Woodworth 2014; hereafter TW), we have argued
49 that large scale variability in the Southern Hemisphere (SH) extratropical flow can be
50 examined in the context of a third type of structure: a *baroclinic* annular mode. The key
51 results of TW are the following:

- 52
- 53 1) The SAM is the leading pattern of variability in the SH *zonal-mean kinetic*
54 *energy*, and it may be viewed as a *barotropic* annular mode. It explains large
55 fractions of the variance in the wave fluxes of momentum, but has a very weak
56 projection onto the eddy fluxes of heat and the eddy kinetic energy.
 - 57 2) In contrast, the leading pattern of variability in the SH *eddy kinetic energy*
58 may be viewed as a *baroclinic* annular mode. Like the SAM, the southern
59 baroclinic annular mode has a distinct zonally symmetric component. But
60 unlike the SAM, it projects strongly onto the eddy fluxes of heat, and only
61 weakly onto the zonal-mean kinetic energy and eddy fluxes of momentum.
 - 62 3) The SAM and its baroclinic counterpart play very different roles in SH climate
63 variability. They have contrasting roles in the extratropical energy cycle. They
64 have very different projections on surface climate. And notably, they have very
65 different signatures in the frequency domain: the SAM can be modeled as
66 Gaussian red noise with a timescale of ~10 days (Hartmann and Lo 1998;
67 Lorenz and Hartmann 2001); the southern baroclinic annular mode exhibits
68 marked variability on ~20-30 timescales (TW; Thompson and Barnes 2014).

70 The purpose of this paper is to extend the analyses of TW to the Northern
71 Hemisphere (NH). We will demonstrate that the NH circulation exhibits a baroclinic
72 annular mode that is very similar to its SH counterpart despite the notable
73 interhemispheric differences in orography and land-sea contrasts. In Section 3, we
74 develop a procedure for identifying baroclinic annular variability in the NH. In Section
75 4, we investigate the signature of the NH baroclinic annular mode in the zonal-mean
76 circulation, and contrast it to the NH barotropic annular mode (the NAM). In Section 5,
77 we examine the longitudinally-varying structure of the NH baroclinic annular mode and
78 examine the teleconnectivity between eddy activity in the North Atlantic and North
79 Pacific stormtrack regions. In Section 6, we examine the spectral characteristics of the
80 NH baroclinic annular mode. Conclusions are provided in Section 7.

81

82 **2. Data/methods**

83 All analyses are based on the European Centre for Medium-Range Weather
84 Forecasts Interim reanalysis data set (ERA-Interim; Dee et al. 2011). The reanalyses
85 output are available on a $1.25^\circ \times 1.25^\circ$ mesh and at 4 x daily resolution. The results are
86 based on daily-mean versions of the data for the period 1979-2011. Daily mean
87 precipitation is calculated by averaging total precipitation at 00 and 12UTC at forecast
88 steps of 6 and 12 hours. Anomalies are formed by subtracting the long-term mean
89 seasonal cycle from the data at all time steps.

90 Throughout the study, brackets denote zonal-mean quantities and $*$ departures from
91 the zonal-mean. The zonal-mean eddy kinetic energy is defined as $\frac{1}{2}[u^*{}^2 + v^*{}^2]$; the
92 zonal-mean eddy fluxes of momentum as $[u^*v^*]$; and the zonal-mean eddy fluxes of heat

93 as $[v^*T^*]$. Eddy fluxes are calculated at $4 \times$ daily resolution and averaged to form daily
94 mean versions of the fluxes.

95 In cases where we use empirical orthogonal function/principal component
96 (EOF/PC) analyses, the data are weighted by the square root of the cosine of latitude
97 and the mass represented by each vertical level in the ERA-Interim before calculating
98 the covariance matrix of the data.

99 As discussed in Section 3, the wind data used to identify baroclinic annular
100 variability are spatially filtered to remove the contributions of planetary-scale eddies to
101 the eddy kinetic energy. Planetary scale eddies are defined here as variations on spatial
102 scales of zonal wavenumbers 1-3; synoptic scale eddies as variations on spatial scales of
103 zonal wavenumbers 4 and higher.

104 Power spectra for time series that span all calendar days are found by: 1) Calculating
105 the spectra for subsets of the time series that are 500 days in length with 250 days
106 overlap between adjacent subsets. Split-cosine-bell tapering is applied to 5% of the data
107 on each end of the subset time series; 2) Averaging the power spectra over all subsets of
108 the time series; and 3) Applying a 3 point running mean to the resulting mean power
109 spectrum. Power spectra for time series limited to the warm and cold seasons are based
110 on subsets that are 183 days in length for the warm season (April-September) and 182
111 days in length for the cold season (October-March) with no overlap between subsets.

112 The statistical significance of the correlation coefficient is assessed using the t -
113 statistic. The confidence levels on the power spectrum are estimated from the Chi-
114 squared distribution and a red-noise fit to the spectrum. As discussed in the Appendix,
115 the lag-one autocorrelations used to estimate the red-noise fits are calculated from high-

116 pass filtered versions of the time series. In the case of correlations, the effective number
117 of degrees of freedom (N^*) are estimated as:

118

$$N^* = N \frac{1 - r_1 r_2}{1 + r_1 r_2} \quad (1)$$

119 where N is the number of time steps used in the correlations, and r_1 and r_2 are the
120 lag-one autocorrelations of the time series being correlated (Bretherton et al. 1999). In
121 the case of power spectra, the degrees of freedom are estimated as the ratio of: 1) the
122 number of time steps in the time series to 2) the number of independent spectral
123 estimates in the power spectrum. Additional details on the significance tests and red-
124 noise fits to the data are provided as necessary in the results sections.

125

126 **3. Defining baroclinic annular variability in the Northern Hemisphere**

127 In this section, we develop an index for characterizing baroclinic annular variability
128 in the NH. Throughout the study, the southern and northern *barotropic* annular modes
129 are denoted as the SAM and NAM, respectively, whereas the southern and northern
130 *baroclinic* annular modes are denoted as the SBAM and NBAM, respectively.

131 The left column in Figure 1 reviews the latitude/lag structure of the southern
132 baroclinic annular mode (the SBAM) in two key fields: the zonal-mean eddy fluxes of
133 heat at 850 hPa and the eddy kinetic energy at 300 hPa. As in TW, the SBAM is defined
134 as the leading PC time series of the zonal-mean eddy kinetic energy for all levels and
135 latitudes within the domain 1000-200 hPa and 20-70°S. By definition, the “positive
136 polarity” of the SBAM is defined as periods when the hemispheric mean eddy kinetic
137 energy is anomalously positive, and vice versa. All results in Figure 1 are based on daily-
138 mean data for all calendar months.

139 Figure 1a shows the unfiltered, zonal mean fields of the eddy fluxes of heat at 850
140 hPa (shading) and the eddy kinetic energy at 300 hPa (contours) regressed onto the
141 SBAM index as a function of lag and latitude. The figure is identical to Figure 3b from
142 TW, but is calculated using a slightly different time period. As noted in that study, the
143 positive polarity of the SBAM is associated with poleward eddy heat flux anomalies and
144 positive eddy kinetic energy anomalies that span much of the SH middle latitudes. The
145 heat flux anomalies precede the eddy kinetic energy anomalies by ~1-2 days, consistent
146 with the time lag between the generation of wave activity in the lower troposphere and
147 the generation of eddy kinetic energy aloft (Simmons and Hoskins 1978).

148 Figures 1c and 1e show the contributions of the synoptic and planetary scale waves to
149 the regressions in the top panel (synoptic and planetary scale waves are defined in
150 Section 2). As evidenced in the left column of Fig. 1, variations in the SBAM are
151 associated almost entirely with eddies on synoptic spatial scales. The dominant role of
152 synoptic scale eddies in association with the SBAM is consistent with: 1) the relatively
153 weak amplitudes of planetary-scale waves in the SH and 2) the notion that the SBAM
154 owes its existence to two-way feedbacks between the baroclinicity and the eddy fluxes of
155 heat by synoptic-scale waves (Thompson and Barnes 2014).

156 The right column in Figure 1 shows analogous results calculated for the NH. In all
157 three panels, the regressions are based on the leading PC time series of the zonal-mean
158 eddy kinetic energy for all levels and latitudes within the domain 1000-200 hPa and 20-
159 70°N. As in the SH, the leading PC of NH eddy kinetic energy is marked by same sign
160 fluctuations in both the eddy kinetic energy and eddy fluxes of heat that span much of
161 the midlatitudes (Fig. 1b). However, unlike the SH, the anomalies have a relatively
162 complicated spatial structure, and derive in roughly equal parts from synoptic and

163 planetary scale eddies (Figs. 1d and 1f). Hence, the leading pattern of variability in the
164 NH eddy kinetic energy field includes a notable contribution from the planetary scale
165 eddies that is not reflected in association with the SBAM.

166 To the extent that baroclinic annular variability reflects the dynamics of baroclinic
167 waves, it follows that a physically meaningful index of baroclinic annular variability
168 should isolate the variance in the eddy kinetic field associated with synoptic-scale
169 eddies. Filtering the eddy kinetic energy field to isolate the variance associated with
170 synoptic-scale eddies is not necessary in the SH, where the planetary-scale waves have
171 relatively weak amplitude. But as evidenced in Fig. 1, it is essential in the NH, where the
172 planetary scale waves make a prominent contribution to the leading EOF of the eddy
173 kinetic energy. For this reason, we will define the time series of the northern baroclinic
174 annular mode (the NBAM) as the leading PC time series of the eddy kinetic energy
175 associated with wavenumbers 4 and higher. As done for the SH, the PC time series is
176 calculated for all levels and latitudes within the domain 1000-200 hPa and 20-70°N.
177 The patterns associated with the resulting NBAM index are explored in the following
178 sections.

179

180 **4. Structure of the NAM and NBAM in the zonal-mean circulation**

181 Figures 2-5 compare the structures of the NAM and NBAM in the extratropical
182 zonal-mean circulation. The NAM index is defined as the leading PC time series of the
183 anomalous daily-mean, zonal-mean zonal wind for all levels and latitudes in the domain
184 1000-200 hPa and 20-70°N. The resulting index is very similar to that used in other
185 studies, e.g., the correlation coefficient between monthly-mean values of the NAM index
186 used here and the leading PC time series of the monthly-mean sea-level pressure field

187 20°-70°N is $r=0.87$. As discussed in the previous section, the NBAM index is defined as
188 the leading PC time series of the eddy kinetic energy associated with zonal wavenumbers
189 4 and higher. The NBAM index explains 43% of the variance in NH synoptic-scale eddy
190 kinetic energy, and both the NAM and NBAM indices are statistically distinct from the
191 second PCs of their respective fields (the variances explained by all PCs considered in
192 this study are listed in Table 1). The positive polarity of the NBAM is defined as periods
193 when the hemispheric mean eddy kinetic energy is anomalously positive, and vice versa.
194 The positive polarity of the NAM is defined as periods when the zonal flow $\sim 55^{\circ}\text{N}$ is
195 anomalous westerly, and vice versa. Unless otherwise noted, the fields regressed on the
196 NBAM and NAM indices are *not* filtered.

197 The NAM and NBAM indices are only weakly correlated at all lags between -20 to
198 + 20 days (not shown) and in 10 day low-pass data (Table 2). Roughly 98% of the
199 variance in the NAM on timescales longer than 10 days is linearly independent of
200 variability in the NBAM.

201
202 *a. Reviewing the signature of the NAM in the zonal-mean tropospheric circulation*

203 The signature of the NAM in the zonal-mean circulation has been examined
204 extensively in previous work (e.g., Thompson and Wallace 2000; Limpasuvan and
205 Hartmann 2000; Lorenz and Hartmann 2003), but is reviewed here for two reasons: 1)
206 to facilitate comparison with the NBAM; and 2) to highlight the surprisingly weak
207 signature of the NAM in the eddy fluxes of heat and eddy kinetic energy.

208 The left column in Fig. 2 reviews the structure of the NAM in the latitude/height
209 plane. The NAM is marked by meridionally banded anomalies in the zonal-mean zonal
210 flow, with primary centers of action located $\sim 30^{\circ}\text{N}$ and $\sim 55^{\circ}\text{N}$ (Fig. 2a; Thompson and

Wallace 2000; Limpasuvan and Hartmann 2000). It is also apparently linked to a third center of action in the zonal-flow near 75°N (contours in Fig. 2a). However, the center of action near 75°N is restricted to the region to the north of Iceland (not shown), is not evident in regressions based on the leading PC of the monthly-mean sea-level pressure (Thompson and Wallace 2000) or zonal wind (Lorenz and Hartmann 2003), and is not clearly mirrored in regressions based on the SAM (e.g., Thompson and Woodworth 2014). The center of action near 75°N is much weaker when the time series used to generate Fig. 2a are 30 day low pass filtered, and is thus mainly associated with NAM-like variability on submonthly timescales.

As reviewed in the left column of Fig. 2, the NAM is also associated with: 1) poleward momentum fluxes centered near the tropopause ~45°N (shading in Fig. 2a; Limpasuvan and Hartmann 2000; Lorenz and Hartmann 2003); 2) negative temperature anomalies at subpolar latitudes juxtaposed against warm temperature anomalies at middle latitudes (shading in Figure 2c; Thompson and Wallace 2000); and 3) paired meridional overturning cells with rising motion at subpolar and tropical latitudes juxtaposed against sinking motion between about 30°-40°N (contours in Fig. 2c). The momentum flux anomalies precede the zonal-wind anomalies by several days, consistent with forcing of the zonal-mean flow by the advection of momentum by the eddies (Fig. 3a; Lorenz and Hartmann 2003). The temperature anomalies associated with the NAM are consistent with adiabatic expansion and compression driven by the attendant changes in vertical motion. The vertical motion anomalies, in turn, are consistent with forcing by the momentum fluxes aloft (Thompson and Wallace 2000). Note that the mass streamfunction has very small amplitude at high latitudes in part due to the relatively small area represented by the polar cap (Fig. 2c).

235 The signatures of the NAM in the zonal wind and eddy fluxes of momentum
236 discussed above are consistent with north-south fluctuations in the axis of the
237 extratropical jet (Lorenz and Hartmann 2003). The signatures of the NAM in the eddy
238 kinetic energy and eddy heat flux anomalies are more difficult to interpret (Fig. 2e). To
239 the extent that variations in the eddy heat fluxes and eddy kinetic energy follow
240 variations in the latitude of the jet, the positive polarity of the NAM should be
241 accompanied not only by anomalously poleward momentum fluxes in the upper
242 troposphere near 45°N, but also by increases in the eddy fluxes of heat and eddy kinetic
243 energy near 55°N and decreases near 30°N. Neither feature is clearly apparent in Fig.
244 2e. As is the case for the SAM (TW), the signature of the NAM in the eddy fluxes of heat
245 is both weak and amorphous throughout most of the midlatitudes (Fig. 2e).

246 The signature of the NAM in the eddy fluxes of heat and momentum is explored
247 further in the left column of Fig. 4. Figure 4a shows the unfiltered eddy fluxes of
248 momentum (contours; reproduced from shading in Fig. 3a) and heat (shading)
249 regressed on the NAM index as a function of lag and latitude. Figures 4c and 4e show
250 the components of the regressions that are due to synoptic (wavenumbers 4 and higher)
251 and planetary-scale (wavenumbers 1-3) waves, respectively. Note that in contrast to the
252 diagnostics presented in DeWeaver and Nigam (2000), Feldstein (2003), and Lorenz
253 and Hartmann (2003), the wave fluxes in Fig. 4 are spatially rather than time filtered.

254 As evidenced in Figs. 4c and 4e, the preponderance of the eddy momentum flux
255 anomalies associated with the NAM are due to variations in synoptic-scale waves. In
256 contrast, a large fraction of the eddy heat flux anomalies associated with the NAM are
257 due to variations in the planetary-scale waves (Fig. 4e), particularly the meridional
258 dipole in eddy heat flux anomalies centered around lag 0. The most pronounced

signature of the NAM in the synoptic-scale wave fluxes of heat is found at positive lag near 50°N (Fig. 4c), and is consistent with the influence of the momentum fluxes aloft on lower tropospheric baroclinicity (Lorenz and Hartmann 2003).

262

263 *b. The signature of the NBAM in the zonal-mean tropospheric circulation*

264 The structure of the NBAM in the extratropical circulation is shown in the right
265 columns of Figs. 2-4. In contrast to the NAM but like its SH counterpart (TW), the
266 NBAM has a weak signature in the zonal-mean zonal wind and wave fluxes of
267 momentum but a pronounced signature in the zonal-mean eddy kinetic energy and wave
268 fluxes of heat (Figs. 2b and 2f). The NBAM is hence associated with hemispheric scale
269 fluctuations in both the generation of eddy kinetic energy in the lower troposphere (as
270 inferred by the vertical gradient in the eddy fluxes of heat near the surface) and eddy
271 amplitudes aloft (as inferred by the eddy kinetic energy). The eddy heat flux anomalies
272 precede the eddy kinetic energy anomalies by ~1-2 days, consistent with the generation
273 of upper tropospheric eddy kinetic energy by developing baroclinic waves in the free
274 troposphere (Fig. 3b; Simmons and Hoskins 1978).

275 Also like its SH counterpart (TW), the NBAM is marked by warm temperature
276 anomalies centered ~50-60°N (shading in Fig. 2d) that are consistent with warming by
277 the anomalously poleward wave fluxes of heat at middle latitudes (shading in Fig. 2f). In
278 contrast to the NAM, the changes in vertical motion are thermally driven (i.e., thermally
279 direct): the midlatitude temperature anomalies are damped rather than driven by the
280 vertical motion anomalies (contours in Fig 2d).

281 In part by construction, the anomalous eddy fluxes of heat and momentum
282 associated with the NBAM are dominated by synoptic scale eddies (right column in Fig.

283 4). Consistent with the barotropic decay stage of baroclinic waves (Simmons and
284 Hoskins 1978), the NBAM is marked by positive anomalies in the wave fluxes of
285 momentum that lag and lie slightly equatorward of the positive anomalies in the wave
286 fluxes of heat (Fig. 4d).

287

288 *c. Summarizing the differences between the NAM and NBAM*

289 As is the case in the SH, the barotropic (the NAM) and baroclinic (the NBAM)
290 northern annular modes have very different signatures in the extratropical circulation.
291 The NAM emerges as the leading PC of the zonal-mean kinetic energy (Table 2). It is
292 driven by the wave fluxes of momentum (Fig. 3a), and has a weak secondary signature
293 in the synoptic-scale wave fluxes of heat that is consistent with the influence of the
294 momentum fluxes upon tropospheric baroclinicity (Fig. 4c; Lorenz and Hartmann
295 2003). The NAM hence explains a large fraction of the variance in the zonal-mean zonal
296 wind and eddy fluxes of momentum (left panels in Fig. 5; solid lines), but a relatively
297 small fraction of the variance in the zonal-mean eddy kinetic energy and eddy fluxes of
298 heat (left panels in Fig. 5; dashed lines).

299 In contrast, the NBAM emerges as the leading EOF of the eddy kinetic energy. It
300 is driven by the wave fluxes of heat (Fig. 3b), and has a secondary signature in the wave
301 fluxes of momentum that is consistent with the baroclinic wave lifecycle (Fig. 4d). The
302 NBAM hence explains a notable fraction of the variance in the zonal-mean eddy kinetic
303 energy and eddy fluxes of heat (right panels in Fig. 5; dashed lines), but a very small
304 fraction of the variance in the zonal-mean zonal wind and eddy fluxes of momentum
305 (right panels in Fig. 5; solid lines). The NBAM explains a smaller fraction of the variance

306 in the eddy kinetic energy than the NAM does in the zonal-mean kinetic energy (bottom
307 panels).

308 The results shown in this section are based on data for all calendar months. The
309 NBAM also emerges as the leading PC of synoptic-scale eddy kinetic energy in analyses
310 performed separately for the warm and cold season months. For example, the
311 correlations between 1) warm season (April-September) segments of the year-round
312 NBAM index and 2) the leading PC of warm season synoptic-scale eddy kinetic energy is
313 $r \sim 0.99$. As is the case for the NAM (Thompson and Wallace 2000), the amplitude of the
314 NBAM is largest during the cold season months.

315 In the following section we will examine the signature of the NBAM in the
316 longitudinally varying circulation and assess the linkages between synoptic-scale eddy
317 kinetic activity in the North Atlantic and North Pacific sectors of the hemisphere.

318

319 **5. Longitudinally-varying aspects of the NBAM**

320 The robust signatures of both the NH and SH baroclinic annular modes in the
321 zonal-mean circulation suggest that they owe their existence to dynamical processes that
322 transcend the land-sea contrasts of their respective hemispheres. In this section, we
323 examine three aspects of the NBAM in the longitudinally-varying circulation: 1) its
324 signature in eddy activity and precipitation; 2) its emergence as the leading pattern of
325 variability in eddy kinetic energy along latitude circles; and 3) its signature in the
326 teleconnectivity between eddy kinetic energy in the two major NH storm track regions.

327

328 *a. The signature of the NBAM in the longitudinally-varying circulation*

329 Figure 6 shows three zonally-varying, daily-mean fields regressed onto
330 standardized daily-mean values of the NBAM index: the eddy-kinetic energy at the 300
331 hPa level (panel a); the eddy-heat fluxes at the 850 hPa level (panel b); and precipitation
332 (panel c). The eddy-heat flux and precipitation results are lagged by minus one day
333 relative to the NBAM index (i.e., the fields peak ~1 day before eddy-kinetic energy peaks
334 in the upper troposphere; see Fig. 3b and also Barnes and Thompson 2014). As in
335 Figures 2 and 3, the eddy fields shown in Fig. 6 are not spatially filtered. The ERA-
336 Interim precipitation is a model-derived quantity but is assumed to provide a physically-
337 consistent, zeroth-order estimate of the linkages with variability in the NBAM.

338 As evidenced in Fig. 6, the positive polarity of the NBAM is associated with
339 anomalously positive eddy-kinetic energy, poleward eddy heat fluxes, and enhanced
340 precipitation over both the North Pacific and North Atlantic sectors of the hemisphere.
341 Over the Pacific sector, the eddy-kinetic energy anomalies peak over the Kuroshio
342 extension region and the central North Pacific, whereas the heat flux anomalies peak
343 over the central and eastern North Pacific. Over the Atlantic sector, the eddy-kinetic
344 energy and eddy-heat flux anomalies peak over the Gulf Stream extension region.
345 Precipitation is enhanced primarily over the Kuroshio and Gulf Stream extension
346 regions.

347 Hence variability in the NBAM is marked by variations in eddy activity that span
348 both major stormtrack regions. In the following subsection, we examine whether the
349 large-scale structure of the NBAM is an artifact of the use of zonal-mean data to define
350 the NBAM index, or whether it also emerges from PC analysis of eddy-kinetic energy
351 anomalies along latitude circles.

352

353 *b. PC analysis of the longitudinally-varying circulation along latitude circles*

354 Figure 7c shows the correlations between a) the leading PC time series of the
355 longitudinally-varying, synoptic-scale eddy kinetic energy calculated as a function of
356 latitude (e.g., at 50°N, the leading PC is calculated for eddy kinetic energy anomalies
357 associated with wavenumbers 4 and higher along 50°N as a function of time and
358 longitude); and b) the NBAM index. Figure 7d shows the corresponding variances
359 explained by the first two PCs of the longitudinally varying synoptic-scale eddy kinetic
360 energy as a function of latitude, where the error bars correspond to the criterion
361 outlined in North et al. (1981). For example, the leading PC of the longitudinally varying
362 synoptic-scale eddy kinetic energy along 50°N is well separated from the second PC at
363 50°N (Fig. 7d), and is correlated with the NBAM index at a level of $r \sim 0.8$ (Fig. 7c).
364 Figures 7a and 7b show corresponding results for the longitudinally varying zonal wind
365 field and the NAM index.

366 The leading PCs of the longitudinally varying synoptic-scale eddy kinetic energy
367 field are highly correlated with the NBAM index throughout middle latitudes (right
368 panels in Fig. 7). Likewise, the leading PCs of the longitudinally varying zonal wind field
369 are strongly correlated with the NAM index time series at latitudes that lie within the
370 primary centers of action of the NAM (left panels in Fig. 7). Hence, the NAM and NBAM
371 correspond to the leading patterns of variability in the longitudinally-varying circulation
372 along latitude circles, and are not an artifact of the zonal averaging performed before
373 calculating the NAM and NBAM indices.

374

375 *c. Teleconnectivity in eddy-kinetic energy between stormtracks*

376 The NBAM exhibits a high degree of annularity across the Pacific and Atlantic
377 sectors of the hemisphere (Fig. 6). In practice, two conditions can lead to an annular-
378 like leading PC in the atmospheric circulation: 1) fluctuations in the circulation must be
379 positively correlated at adjacent grid boxes (though not necessarily between widely
380 separate longitudes) and 2) the variance of the circulation must exhibit a high degree of
381 zonal symmetry (Gerber and Vallis 2005). Neither condition requires zonally coherent
382 fluctuations in the flow, and hence an annular-like leading PC can arise even in the
383 absence of significant positive correlations between variability in the circulation over the
384 two stormtrack regions. In a companion study (Gerber and Thompson, in preparation),
385 we examine the conditions under which the NBAM reflects zonally coherent fluctuations
386 in the flow. Below we examine the structure of the NBAM over both major NH storm
387 track regions and explore the teleconnectivity in eddy kinetic energy between them.

388 First, we examine to what extent the structure of the NBAM emerges from
389 analyses of the circulation over the North Atlantic and North Pacific sectors of the
390 hemisphere. The results in Fig. 8 are identical to those shown in the right column of Fig.
391 2, but are derived from analyses restricted to 90°W-50°E (the North Atlantic sector) and
392 110°E-110°W (the North Pacific sector). For example: The NBAM_{Atlantic} index is defined
393 as the leading PC of the synoptic-scale eddy-kinetic energy from 1000-200 hPa averaged
394 90°W-50°E, and the results in the left column of Fig. 8 show unfiltered data averaged
395 90°W-50°E regressed on standardized values of the NBAM_{Atlantic} index. The right
396 column shows analogous results calculated for the North Pacific sector. The results in
397 Figure 8 are not sensitive to the specific boundaries used to designate the Pacific and
398 Atlantic sectors of the hemisphere.

399 The key result in Fig. 8 is that the leading patterns of variability in the amplitude
400 of synoptic-scale eddy activity in the Atlantic and Pacific sectors of the NH both bear a
401 strong resemblance to the NBAM. Both are marked by a monopole in the eddy fluxes of
402 heat and eddy kinetic energy centered \sim 40-45°N (Figs. 8e and 8f; the eddy kinetic
403 energy anomalies associated with the NBAM_{Atlantic} index are shifted slightly poleward of
404 their Pacific counterparts); both exhibit positive temperature anomalies that peak
405 \sim 400hPa near 50°N (Figs. 8c and 8d); and both have a relatively weak signature in the
406 zonal wind field (Figs. 8a and 8b). The similarities between the leading modes of eddy
407 kinetic energy over the two stormtrack regions is surprising considering the notable
408 differences in the climatology of the two sectors.

409 The NBAM_{Atlantic} and NBAM_{Pacific} indices are correlated with the NBAM index at
410 levels of $r=0.67$ and $r=0.72$. Hence they contribute roughly equally to variations in the
411 NBAM index. The NBAM_{Atlantic} and NBAM_{Pacific} indices are also significantly linked to
412 each other. Figure 9 shows the correlations between the NBAM_{Atlantic} and NBAM_{Pacific}
413 indices as a function of lag. The leading patterns of synoptic-scale eddy kinetic energy
414 over the North Pacific sector and North Atlantic sectors are significantly linked to each
415 other, particularly when the North Pacific sector leads the North Atlantic sector by \sim 3-4
416 days. The correlations between the two sectors are most pronounced during the cold
417 season months (not shown).

418 The linkages between eddy kinetic energy in the two storm track regions are
419 further evidenced in the lag regressions of (unfiltered) eddy-kinetic energy at the 300
420 hPa level onto the NBAM_{Pacific} index. At lag 0 (Fig. 10a), the eddy kinetic energy
421 anomalies associated with the NBAM_{Pacific} index have large amplitude over the Pacific
422 sector but do not project onto eddy kinetic energy over the North Atlantic sector. At

423 successive lags, the eddy kinetic anomalies not only decay over the Pacific sector, but
424 also appear to propagate across North America towards the North Atlantic in a manner
425 consistent with that shown in Chang and Yu (1999) and Li and Lau (2012). Roughly ~3-
426 4 days after peak amplitude in the NBAM_{Pacific} index (panels d and e), the North Atlantic
427 stormtrack is marked by positive - albeit relatively weak - anomalies in eddy kinetic
428 energy centered over the Gulf Stream extension region. The linkages between eddy
429 kinetic energy in the Pacific sector and over the Gulf Stream extension region ~3-4 days
430 later are statistically significant at the 99% confidence level (Figs. 10d, 10e and 11). The
431 downstream development of eddy-kinetic energy anomalies across Asia towards the
432 North Pacific is much less clear (not shown).

433 Several studies have argued that variations in upper tropospheric baroclinic
434 activity in the two stormtracks are significantly correlated (e.g., Chang and Fu 2002;
435 Chang 2004; Li and Lau 2012). But others have noted that the correlations between the
436 stormtracks are very weak (Wettstein and Wallace 2010). The results shown in Figs. 9-11
437 confirm that the linkages between upper-tropospheric variability in the stormtracks are
438 weak. But they also confirm that the linkages are significant, particularly when the
439 North Pacific stormtrack leads the North Atlantic stormtrack by several days. To what
440 extent the weak but significant propagation of eddy kinetic energy from the North
441 Pacific to North Atlantic storm tracks contributes to the zonally symmetric structure of
442 the NBAM is examined in the companion study (Gerber and Thompson, in preparation).
443

444 **6. Quasi-periodic behavior in the NBAM**

445 The southern baroclinic annular mode exhibits quasi-periodic variability on
446 timescales of ~20-30 days (TW). The quasi-periodic behavior in the SBAM is consistent

447 with two-way feedbacks between the extratropical baroclinicity and the eddy fluxes of
448 heat by baroclinic waves, and extends to large-scale averages of eddy kinetic energy, the
449 eddy fluxes of heat, and precipitation (Thompson and Barnes 2014). Below we
450 investigate to what extent analogous quasi-periodic behavior is evident in association
451 with the NBAM.

452 Figure 12 shows the power spectrum of the NBAM index calculated for data for
453 all calendar months (details of the calculation are provided in Section 2). The NBAM
454 index time series exhibits enhanced spectral power centered around \sim 25 days (\sim 0.04
455 cpd). The peak in the spectrum is weaker than the corresponding peak in the SBAM
456 (TW, c.f. Fig. 12). But it is reproducible in subsets of the data (Appendix Fig. A1) and is
457 statistically significant at the 99% level based on the Chi-squared statistic applied to a
458 red-noise fit to the spectrum (see Section 2 and the Appendix for details of the
459 significance tests). Interestingly, the spectral peak in the NBAM index derives almost
460 entirely from the summer season, as evidenced in the top panels in Fig. 13. Both the
461 pronounced spectral peak during summer and the lack of a robust peak during winter
462 are reproducible in both halves of the data record (Appendix Fig. A1). The lack of a
463 robust peak during the cold season is consistent with Ambaum and Novak (2013), who
464 did not find evidence of statistically significant periodicity in the North Atlantic
465 stormtrack during the winter season.

466 The spectral peak in the NBAM during the warm season months extends to
467 various indices of synoptic eddy activity. It is apparent in the spectrum of the
468 hemispheric-mean synoptic-scale eddy kinetic energy at 300 hPa (not shown; the
469 spectrum is largely identical to that for the NBAM index). And it is apparent in the

470 spectrum of the hemispheric-mean eddy fluxes of heat by synoptic-scale eddies (Fig. 13
471 c).

472 The spectral peak in the NBAM is statistically significant, reproducible in subsets
473 of the data, and evident in the eddy fluxes of heat. However, for the most part, it is less
474 robust than its SH counterpart. The peak in the NBAM and its seasonality are not
475 reproducible in the same coupled atmosphere/ocean climate model that readily
476 simulates the peak in the SBAM (the GFDL CM3; Thompson and Barnes 2014). The
477 peak in the NBAM is not apparent in data restricted to the North Atlantic and North
478 Pacific stormtrack regions (i.e., it is not evident in the NBAM_{Atlantic} and NBAM_{Pacific}
479 indices). And the peak in the NBAM and its seasonality are not clearly reproducible in
480 NH-mean precipitation (the peak in the SBAM clearly extends to SH-mean
481 precipitation; Thompson and Barnes 2014). The spectral peak in the NBAM will be
482 examined in more detail in a companion paper.

483

484 **7. Concluding remarks**

485 The NBAM is remarkably similar to its SH counterpart despite the pronounced
486 differences in the land/sea geometry of the two hemispheres (Fig. 14). Both are
487 characterized by hemispheric-scale monopoles in the eddy kinetic energy and eddy
488 fluxes of heat (Fig. 14, bottom). Both have very weak signatures in the wave fluxes of
489 momentum and the zonal-mean zonal flow (Fig. 14, top). And both are associated with
490 changes in vertical motion and temperature that are consistent with the circulation
491 response to the anomalous fluxes of heat (Fig. 14, middle, i.e., the regions poleward of
492 the maximum heat flux anomalies are marked by anomalously warm conditions and
493 anomalous rising motion).

494 The NBAM is also reminiscent of the leading patterns of stormtrack variability
495 identified in previous work. A large-scale monopole in the amplitude eddy activity also
496 emerges from PC analyses of: 1) the variance of the 10 day high-pass filtered upper
497 tropospheric meridional wind (Wettstein and Wallace 2010), 2) the rms 2.5-6 day band-
498 pass filtered middle tropospheric geopotential height field (Lau 1988), and 3) the 8 day
499 high-pass filtered 850 hPa meridional eddy heat flux (Nakamura et al. 2002). A key
500 distinction between the NBAM and the modes of pulsing stormtrack activity identified
501 in previous studies lies in their zonal scales. Wettstein and Wallace (2010) note that the
502 linkages between variability in the North Pacific and North Atlantic stormtracks are very
503 weak, and thus focus primarily on patterns of stormtrack activity within the two ocean
504 basins. The results shown here suggest that the linkages between eddy kinetic energy in
505 the Pacific and Atlantic stormtrack regions are statistically significant. In a companion
506 study (Gerber and Thompson in preparation), we examine to what extent the weak but
507 significant correlations between eddy kinetic energy over the two stormtrack regions
508 contribute to the hemispheric-scale structure of the NBAM.

509 A notable distinction between the analyses used to identify baroclinic annular
510 variability in the Southern and Northern Hemispheres lies in the filtering of the wave
511 fluxes. The baroclinic annular modes are consistent with two-way feedbacks between
512 the baroclinicity and the wave fluxes of heat by synoptic-scale waves (Thompson and
513 Barnes 2014). In the SH, the total variance in the eddy kinetic energy is dominated by
514 waves on synoptic scales and thus the SBAM emerges from PC analysis of the full eddy
515 kinetic energy field. However, in the NH the total variance in the eddy kinetic energy
516 field includes a substantial contribution from the planetary-scale waves. For this reason,

517 the NBAM emerges most clearly from PC analysis of the eddy kinetic energy field after
518 the variance due to planetary-scale waves has been filtered from the data.

519 As is the case in the SH, the two primary NH annular modes play very different
520 roles in cycling energy through the NH circulation. The baroclinic annular mode (the
521 NBAM) is linked primarily to variability in 1) the conversions between available zonal-
522 mean and eddy potential energy and 2) the eddy kinetic energy (Fig. 5 right). The
523 barotropic annular mode (the NAM) is linked primarily to variability in 1) the
524 conversions between eddy and zonal-mean kinetic energy and 2) the zonal-mean kinetic
525 energy (Fig. 5 left). The NBAM exhibits statistically significant periodicity on timescales
526 of ~20-25 days that is most clear during the summer season. But the spectral peak in the
527 NBAM index is generally less robust than that associated with the SBAM. We are
528 currently investigating the climate impacts of the NBAM and the implications of its
529 periodic behavior for NH climate variability.

530

531 **Acknowledgments**

532 We thank John M. Wallace and two anonymous reviewers for their helpful
533 comments on the manuscript. DWJT is funded by the NSF Climate Dynamics program.
534 YL is funded by CloudSAT via NASA JPL and the NSF Climate Dynamics program.

535

536 **Appendix**

537 *Red-noise fits to the power spectra*

538 The broad spectral peak at low frequencies in the NBAM index contributes to its
539 lag-one autocorrelation. As such, the red-noise fit based on the lag-one autocorrelation
540 of the NBAM index is distorted towards the low-frequency end of the spectrum. For
541 example, Fig. A2 shows the spectrum of the NBAM index reproduced from Fig. 12. The
542 red-noise fit indicated by the solid line is based on the lag-one autocorrelation of the
543 unfiltered NBAM index. It clearly overestimates the amount of power in the red-noise fit
544 at low frequencies but underestimates the amount of power in the fit at high frequencies
545 (the area under the fit is equal to the area under the NBAM spectrum).

546 The component of the NBAM index that can be modeled as red-noise is best
547 estimated from the lag-one autocorrelation of the NBAM index after it has been filtered
548 to remove the broad spectral peak at low frequencies. The dashed line in Fig. A2 shows
549 the red-noise fit based on the lag-one autocorrelation of the 20-day high-pass filtered
550 NBAM index. The resulting red-noise fit evidently provides a much more realistic
551 “background” spectrum against which the peak at low frequencies can be tested. The
552 red-noise fit in Fig. 12 is based on the lag-one autocorrelation of 20-day high-pass
553 filtered data; the red-noise fits in Fig. 13 are based on the lag-one autocorrelations of
554 30-day high-pass filtered data.

555

556

- 557 **References**
- 558 Ambaum, M. H. P., and L. Novak, 2014: A nonlinear oscillator describing storm track
559 variability. *Quart. J. Roy. Meteor. Soc.*, 139. doi:10.1002/qj.2352.
- 560 Bretherton, C. S., M. Widmann, V. P. Dymnikov, J. M. Wallace, and I. Blade, 1999: The
561 effective number of spatial degrees of freedom of a time-varying field. *J. Climate*, 12,
562 1990–2009.
- 563 Chang, E. K. M., and D. B. Yu, 1999: Characteristics of wave packets in the upper
564 troposphere. Part I: Northern Hemisphere winter. *J. Atmos. Sci.*, 56, 1708–1728.
- 565 Chang, E. K. M., and Y. Fu, 2002: Interdecadal variations in Northern Hemisphere
566 winter storm track intensity. *J. Climate*, 15, 642–658.
- 567 Chang, E. K. M., 2004: Are the Northern Hemisphere winter storm tracks significantly
568 correlated? *J. Climate*, 17, 4230–4244.
- 569 Dee, D. P., and Coauthors, 2011: The ERA-Interim reanalysis: Configuration and
570 performance of the data assimilation system. *Quart. J. Roy. Meteor. Soc.*, 137, 553–
571 597, doi:10.1002/qj.828.
- 572 DeWeaver, E. and S. Nigam, 2000: Do Stationary Waves Drive the Zonal-Mean Jet
573 Anomalies of the Northern Winter? *J. Climate*, 13, 2160–2176.
- 574 Feldstein, S. B., 2003: The dynamics of NAO teleconnection pattern growth and decay.
575 *Quarterly Journal of the Royal Meteorological Society* 129:589, 901–924
- 576 Gerber, E. P., and G. K. Vallis, 2005: A Stochastic Model for the Spatial Structure of
577 Annular Patterns of Variability and the North Atlantic Oscillation. *J. Climate*, 18,
578 2102–2118.
- 579 Hartmann, D. L. and F. Lo, 1998: Wave-driven zonal flow vacillation in the Southern
580 Hemisphere. *J. Atmos. Sci.*, 55, 1303–1315.

- 581 Hurrell, J. W., 1995: Decadal trends in the North Atlantic Oscillation: Regional
582 temperatures and precipitation. *Science*, **269**, 676–679.
- 583 Kidson, J. W., 1988: Interannual variations in the Southern Hemisphere circulation. *J.*
584 *Climate*, **1**, 1177–1198.
- 585 Lau, N.-C., 1988: Variability of the observed midlatitude storm tracks in relation to low-
586 frequency changes in the circulation pattern. *J. Atmos. Sci.*, **45**, 2718–2743.
- 587 Li, Y., and N.-C. Lau, 2012: Contributions of Downstream Eddy Development to the
588 Teleconnection between ENSO and the Atmospheric Circulation over the North
589 Atlantic. *J. Climate*, **25**, 4993–5010.
- 590 Limpasuvan, V. and D. L. Hartmann, 2000: Wave-maintained annular modes of climate
591 variability. *J. Climate*, **13**, 4414–4429.
- 592 Lorenz, D. J. and D. L. Hartmann, 2001: Eddy-zonal flow feedback in the Southern
593 Hemisphere. *J. Atmos. Sci.*, **58**, 3312–3327.
- 594 Lorenz, D. J., and D. L. Hartmann, 2003: Eddy–zonal flow feed- back in the Northern
595 Hemisphere winter. *J. Climate*, **16**, 1212– 1227.
- 596 Limpasuvan, V. and D. L. Hartmann, 2000: Wave-maintained annular modes of climate
597 variability. *J. Climate*, **13**, 4414–4429.
- 598 Nakamura, H., T. Izumi, and T. Sampe, 2002: Interannual and decadal modulations
599 recently observed in the Pacific storm track activity and East Asian winter monsoon.
600 *J. Climate*, **15**, 1855–1874
- 601 North, G. R., T. L. Bell, R. F. Cahalan, and F. J. Moeng, 1982: Sampling errors in the
602 estimation of empirical orthogonal functions. *Mon. Wea. Rev.*, **110**, 699–706.
- 603 Quadrelli, R., and J. M. Wallace, 2004: A simplified linear frame- work for interpreting
604 patterns of Northern Hemisphere wintertime climate variability. *J. Climate*, **17**,

- 605 3728–3744.
- 606 Simmons, A. J., and B. J. Hoskins, 1978: The life cycles of some nonlinear baroclinic
607 waves. *J. Atmos. Sci.*, 35, 414–432.
- 608 Thompson, D. W. J., and J. M. Wallace, 2000: Annular modes in the extratropical
609 circulation. Part I: Month-to-month variability. *J. Climate*, 13, 1000–1016.
- 610 Thompson, D. W. J., and E. A. Barnes, 2014: Periodic Variability in the Large-Scale
611 Southern Hemisphere Atmospheric Circulation. *Science*, 343, 641-645.
- 612 Thompson, D. W. J., and J. D. Woodworth, 2014: Barotropic and baroclinic annular
613 variability in the Southern Hemisphere. *J. Atmos. Sci.*, 71, 1480-1493.
- 614 Wallace, J. M., 2000: North Atlantic Oscillation/Annular Mode: Two paradigms—One
615 phenomenon. *Quart. J. Roy. Meteor. Soc.*, 126, 791–805.
- 616 Wallace, J. M., and D. S. Gutzler, 1981: Teleconnections in the geopotential height field
617 during the Northern Hemisphere winter. *Mon. Wea. Rev.*, 109, 784–812.
- 618 Wettstein, J.J., and J.M. Wallace, 2010: Observed Patterns of Month-to-Month Storm
619 Track Variability and Their Relationship to the Background Flow. *J. Atmos. Sci.*, 67,
620 1420-1437.
- 621

622 **Tables**

623 **Table 1:** Variance explained by the PCs considered in this study. The PCs are calculated
 624 for zonal-mean, daily-mean data between 1000–200 hPa and 20°–70°N for the fields
 625 indicated. ZKE denotes the zonal-mean kinetic energy; EKE_{WN4+} the zonal-mean eddy
 626 kinetic energy associated with zonal wavenumbers 4 and higher; Atlantic and Pacific
 627 denote data restricted to longitude bands 90°W–50°E, and 110°E–110°W, respectively;
 628 cold and warm denote data restricted to October–March and April–September,
 629 respectively. All leading PCs are well separated from the second PC as per the criterion
 630 outlined in North et al. (1982).

631

Variances explained

	U	ZKE	EKE _{WN4+}	EKE _{WN4+} ^{Atlantic}	EKE _{WN4+} ^{Pacific}	EKE _{WN4+} ^{Cold}	EKE _{WN4+} ^{Warm}
	(NAM)	(NBAM)					
PC 1	34.1	37.0	43.0	42.2	47.5	45.4	40.9
PC 2	25.4	27.1	18.3	19.5	16.3	16.7	18.5

632

633

634

635

636

637

638 **Table 2:** Correlations between the leading PCs of the fields indicated. The PCs are
639 described in association with Table 1. Correlations are computed between 10-day low
640 pass filtered versions of the PC time series. Bold font indicates results that are
641 significant at the 99% confidence level based on a two-tailed test of the *t*-statistic.

642

643

Correlation coefficients

	PC 1 EKE _{WN4+} (NBAM)	PC1 ZKE	PC1 U (NAM)
PC 1 EKE _{WN4+} (NBAM)	1	0.15	0.15
PC1 ZKE	0.15	1	0.85

644

645

646 **Figure Captions**

647 **Figure 1:** Latitude/lag structure of the leading PCs of eddy kinetic energy (EKE) in the
648 Southern Hemisphere (SH; left) and Northern Hemisphere (NH; right). Results are
649 based on daily-mean data for all calendar months. (top) Daily-mean, zonal-mean values
650 of the eddy fluxes of heat at 850 hPa (shading) and EKE at 300 hPa (contours)
651 regressed onto the leading PC time series of EKE. The PC time series are derived from
652 analysis of unfiltered EKE within 1000-200 hPa and 20°-70°. (middle and bottom)
653 Components of the regressions in the top panels that derive from synoptic (zonal
654 wavenumbers 4 and higher) and planetary scale (zonal wavenumbers 1-3) waves.
655 Negative lags denote the field leads the PC time series, and vice versa. Contour intervals
656 are $-3.5, 3.5, 10.5 \dots \text{m}^2 \text{s}^{-2}$.

657

658 **Figure 2:** Vertical structure of the northern annular mode (NAM) and northern
659 baroclinic annular mode (NBAM) in the zonal-mean circulation. Results show daily-
660 mean, zonal-mean values of the fields indicated regressed on standardized values of the
661 NAM (left) and NBAM (right) indices. The NAM index is defined as the leading PC time
662 series of NH zonal-mean zonal wind. The NBAM index is defined as the leading PC of
663 NH synoptic-scale zonal-mean eddy kinetic energy. Results are based on daily-mean
664 data for all calendar months. Regression coefficients are based on contemporaneous
665 values of the data, except in the cases of $[u^*v^*]$ and $[v^*T^*]$, in which the fluxes lead the
666 NAM and NBAM indices by 1 day. Contour intervals are $-0.5, 0.5, 1.5 \dots \text{m s}^{-1}$
667 (top); $-0.5, 0.5, 1.5 \times 10^9 \text{ kg s}^{-1}$ (middle); $-3, 3, 9 \dots \text{m}^2 \text{s}^{-2}$ (bottom). Solid and dashed
668 contours denote clockwise and counterclockwise motion in the middle panels.

669

670 **Figure 3:** Latitude/lag structure of NAM and NBAM in zonal-mean kinetic energy.

671 Results show daily-mean, zonal-mean values of the fields indicated regressed on

672 standardized values of the NAM (left) and NBAM (right) indices as a function of latitude

673 and lag. The momentum fluxes, zonal wind and eddy kinetic energy are shown at 300

674 hPa. The heat fluxes are shown at 850 hPa. Negative lags denote the field leads the base

675 index, and vice versa. Contours are shown at $-0.35, 0.35, 1.5 \dots \text{m s}^{-1}$ (left); $-3.5, 3.5,$

676 $10.5 \dots \text{m}^2 \text{s}^{-2}$ (right).

677

678 **Figure 4:** Wavenumber breakdown of the latitude/lag structure of NAM and NBAM in

679 the eddy fluxes of heat and momentum. Results show daily-mean, zonal-mean values of

680 the fields indicated regressed on standardized values of the NAM (left) and NBAM

681 (right) indices as a function of latitude and lag. (top) unfiltered data (reproduced from

682 the corresponding results in Fig. 3). (middle and bottom) the components of the

683 regressions in the top panels that are due to synoptic (zonal wavenumbers 4 and higher)

684 and planetary scale (zonal wavenumbers 1-3) waves. Negative lags denote the field leads

685 the base index, and vice versa. Contour interval is $4 \text{ m}^2 \text{s}^{-2}$.

686

687 **Figure 5:** Percent variance explained by the NAM (left) and NBAM (right) in vertically

688 averaged values of the indicated fields. The time series and data are 10 day low-pass

689 filtered to emphasize covariability on timescales longer than those associated with a

690 typical baroclinic wave. The fields are vertically averaged between 950 and 250 hPa.

691

692 **Figure 6:** Horizontal structure of the NBAM in EKE, the eddy fluxes of heat and

693 precipitation. Results show daily-mean eddy kinetic energy at 300 hPa (top), the eddy

694 fluxes of heat at 850 hPa (middle) and precipitation (bottom) regressed onto
695 standardized values of NBAM index. The heat fluxes and precipitation lead the NBAM
696 index by 1 day.

697

698 **Figure 7:** (a) Correlations between the NAM index and the leading PCs of the daily-
699 mean, longitudinally-varying zonal wind. The PCs are calculated as a function of
700 latitude. (b) Variances explained by the first and second PCs of the daily-mean,
701 longitudinally-varying zonal wind. (c) As in (a), but for correlations between the NBAM
702 index and the leading PCs of daily-mean, synoptic-scale eddy kinetic energy. (d) As in
703 (b), but for the PCs of the daily-mean, synoptic-scale eddy kinetic energy. Error bars are
704 derived from the significance test described in North et al. (1982). The PCs are
705 calculated based on daily-mean data. The correlations are based on 10 day low-pass
706 versions of the time series to emphasize covariability on timescale longer than those
707 associated with a typical baroclinic wave.

708

709 **Figure 8:** Structure of baroclinic annular variability over the North Atlantic and North
710 Pacific sectors of the hemisphere. As in the right column of Figure 2, but for results
711 calculated separately for the Atlantic (left; 90°W-50°E) and Pacific (right; 110°E-110°W)
712 sectors of the hemisphere. The NBAM_{Atlantic} is defined as the leading PC time series of
713 synoptic-scale EKE in the Atlantic sector from 1000-200 hPa; the NBAM_{Pacific} index as
714 the leading PC time series of synoptic-scale EKE in the Pacific sector from 1000-200
715 hPa.

716

717 **Figure 9:** Lead/lag correlations between the NBAM_{Pacific} index and NBAM_{Atlantic} index.
718 Negative lags denote the NBAM_{Atlantic} index leads the NBAM_{Pacific}, and vice versa. The
719 horizontal dashed line indicates the 99% significance level based on a two-tailed test of
720 the *t*-statistic.

721
722 **Figure 10:** Regressions of eddy kinetic energy at 300 hPa onto the NBAM_{Pacific} index as
723 a function of lag. Stippling indicates results that exceed 99% confidence level based on a
724 two-tailed test of the *t*-statistic.

725
726 **Figure 11:** As in Fig. 9, but for lead/lag correlations between the NBAM_{Pacific} index and
727 eddy kinetic energy at 300 hPa averaged over Gulf Stream extension region (see black
728 borders indicated in Fig. 10e). Horizontal line indicates 99% significance levels based on
729 a two-tailed test of the *t*-statistic.

730
731 **Figure 12:** Power spectra of the NBAM index calculated from daily-mean data for all
732 calendar days. Solid and dashed lines indicate a) the red noise fit to the 20-day high
733 pass filtered NBAM index and b) the 99% confidence level, respectively. See text and
734 Appendix for details of the calculation.

735
736 **Figure 13:** Power spectra of the NBAM index (top) and the synoptic-scale eddy fluxes
737 of heat at 850 hPa averaged 30° to 70°N (bottom). Results are calculated based on daily-
738 mean data during the warm (left) and cold (right) seasons. Warm and cold seasons are
739 defined as April–September, and October–March, respectively. Solid and dashed lines
740 indicate a) the red noise fit to the 30-day high pass filtered time series and b) the 99%

741 confidence levels, respectively. See text for details of the calculation. Note that the
742 differences in spectral resolution between the results shown in Figs. 12 and 13 are due to
743 the different subset lengths used in the calculations (Section 2).

744

745 **Figure 14:** Comparing the vertical structures of the southern and northern baroclinic
746 annular modes. Results show daily-mean, zonal-mean values of the fields indicated
747 regressed on standardized values of the SBAM (left) and NBAM (right) indices. Results
748 for the NBAM are reproduced from Fig. 2 (right column). Results for the SBAM are
749 reproduced from TW (but based on the period of record January 1979-December 2011).

750

751 **Figure A1.** As in Fig. 12 and Fig. 13 (top row), but left panels show spectra of the
752 NBAM for the first half of the data record, and right panels show spectra for the second
753 half of the data record.

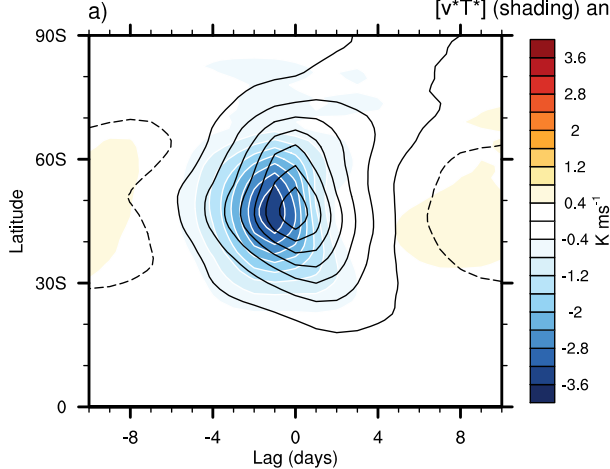
754

755 **Figure A2.** The power spectrum of the NBAM index is reproduced from Fig. 12. Solid
756 and dashed lines indicate the red noise fits to the a) unfiltered NBAM index and b) 20-
757 day high pass filtered NBAM index, respectively.

758

759

Regressions on leading PC of EKE: SH



Regressions on leading PC of EKE: NH

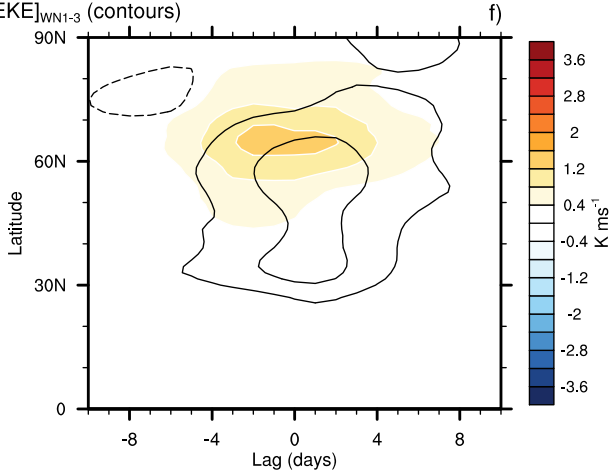
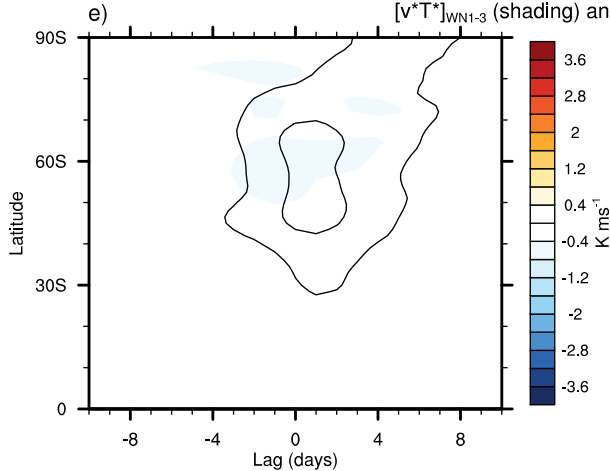
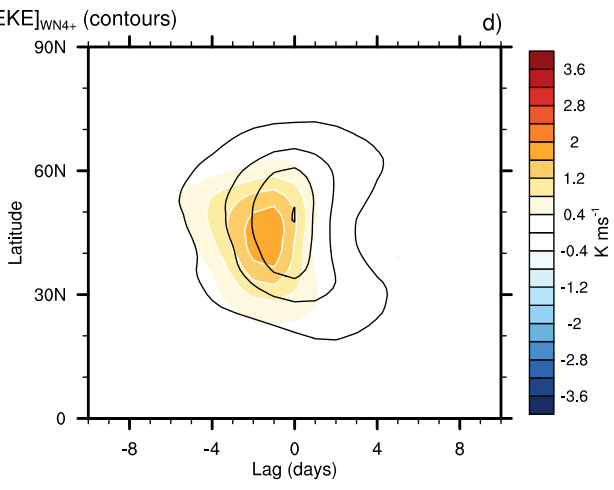
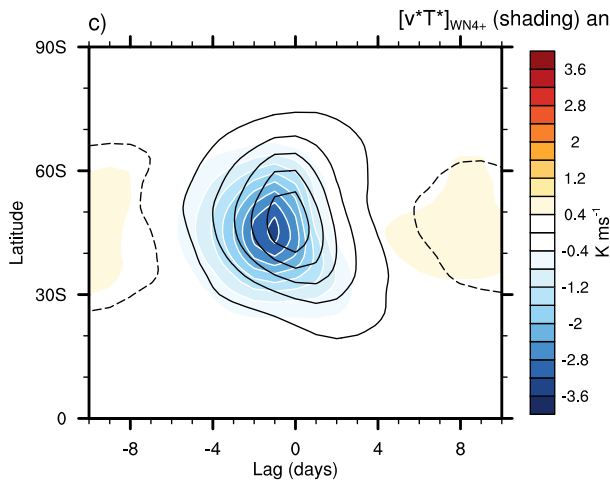
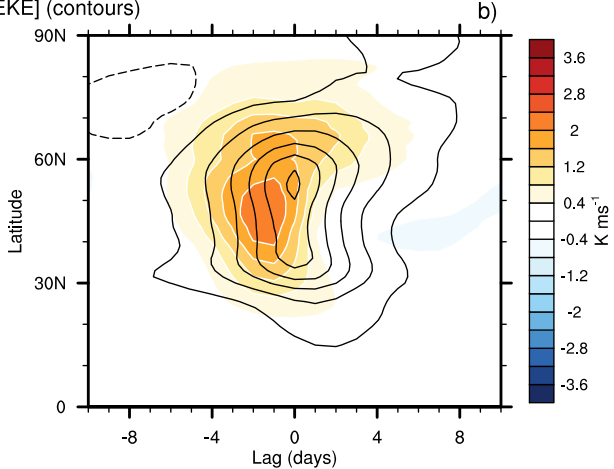


FIG. 1. Latitude/lag structure of the leading PCs of eddy kinetic energy (EKE) in the Southern Hemisphere (SH; left) and Northern Hemisphere (NH; right). Results are based on daily-mean data for all calendar months. (top) Daily-mean, zonal-mean values of the eddy fluxes of heat at 850 hPa (shading) and EKE at 300 hPa (contours) regressed onto the leading PC time series of EKE. The PC time series are derived from analysis of unfiltered EKE within 1000–200 hPa and 20° – 70° . (middle and bottom) Components of the regressions in the top panels that derive from synoptic (zonal wavenumbers 4 and higher) and planetary scale (zonal wavenumbers 1–3) waves. Negative lags denote the field leads the PC time series, and vice versa. Contour intervals are $-3.5, 3.5, 10.5 \dots \text{m}^2 \text{s}^{-2}$.

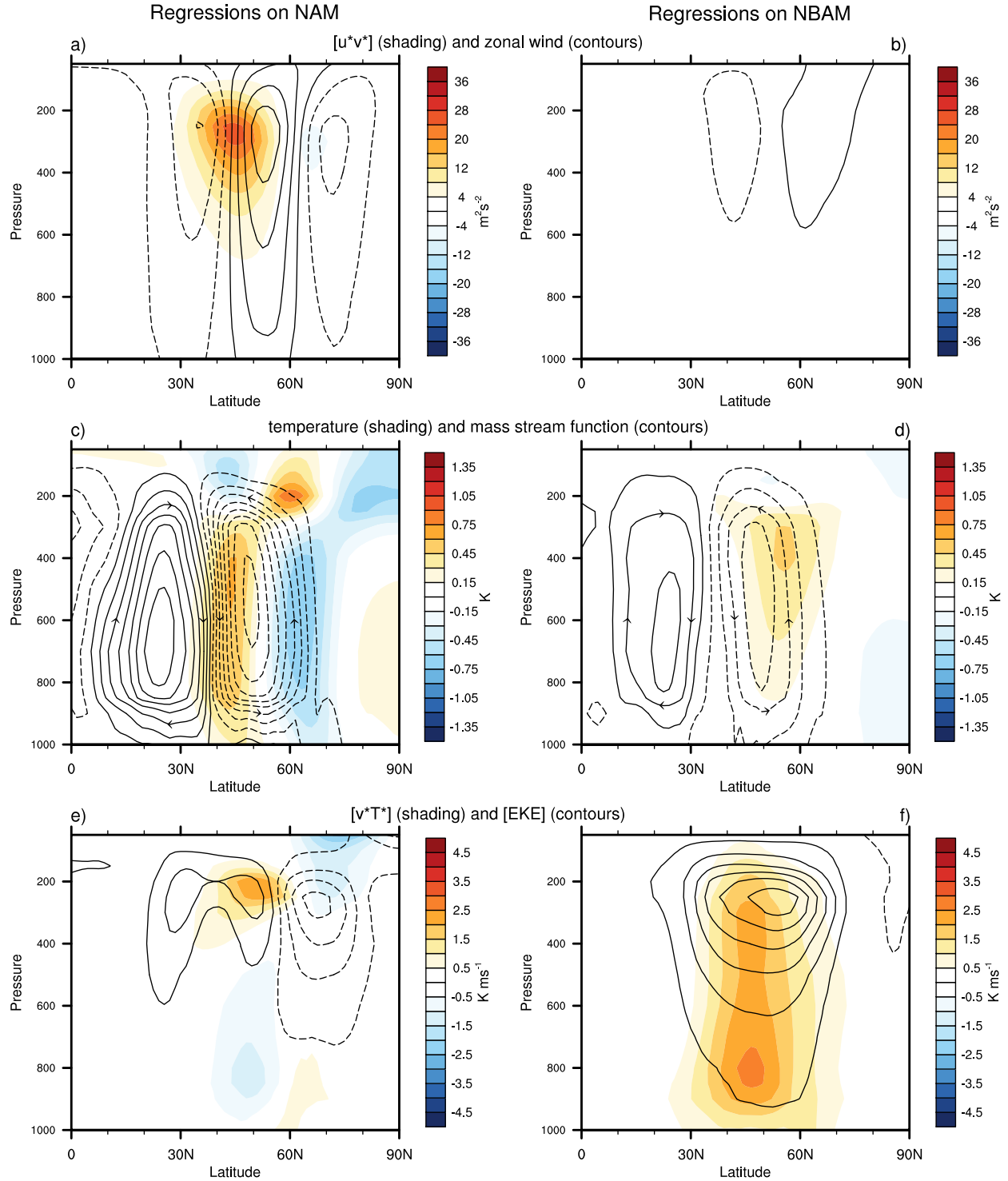


FIG. 2. Vertical structure of the northern annular mode (NAM) and northern baroclinic annular mode (NBAM) in the zonal-mean circulation. Results show daily-mean, zonal-mean values of the fields indicated regressed on standardized values of the NAM (left) and NBAM (right) indices. The NAM index is defined as the leading PC time series of NH zonal-mean zonal wind. The NBAM index is defined as the leading PC of NH synoptic-scale zonal-mean eddy kinetic energy. Results are based on daily-mean data for all calendar months. Regression coefficients are based on contemporaneous values of the data, except in the cases of $[u^*v^*]$ and $[v^*T^*]$, in which the fluxes lead the NAM and NBAM indices by 1 day. Contour intervals are $-0.5, 0.5, 1.5 \dots \text{m s}^{-1}$ (top); $-0.5, 0.5, 1.5 \times 10^9 \text{ kg s}^{-1}$ (middle); $-3, 3, 9 \dots \text{m}^2 \text{s}^{-2}$ (bottom). Solid and dashed contours denote clockwise and counterclockwise motion in the middle panels.

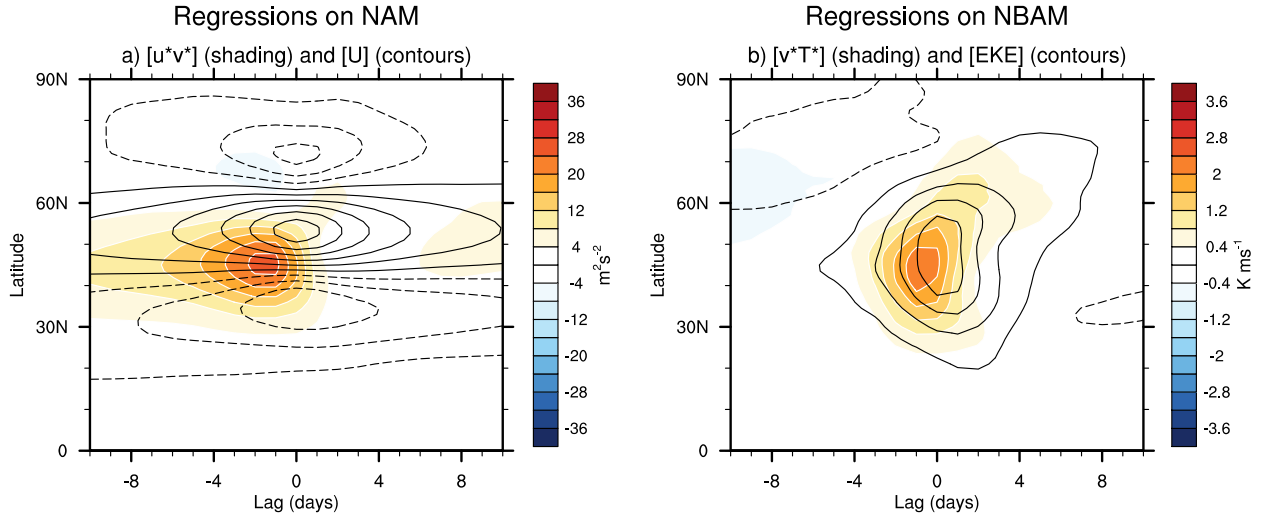


FIG. 3. Latitude/lag structure of NAM and NBAM. Results show daily-mean, zonal-mean values of the fields indicated regressed on standardized values of the NAM (left) and NBAM (right) indices as a function of latitude and lag. The momentum fluxes, zonal wind and eddy kinetic energy are shown at 300 hPa. The heat fluxes are shown at 850 hPa. Negative lags denote the field leads the base index, and vice versa. Contours are shown at $-0.35, 0.35, 1.5 \dots \text{m s}^{-1}$ (left); $-3.5, 3.5, 10.5 \dots \text{m}^2 \text{s}^{-2}$ (right).

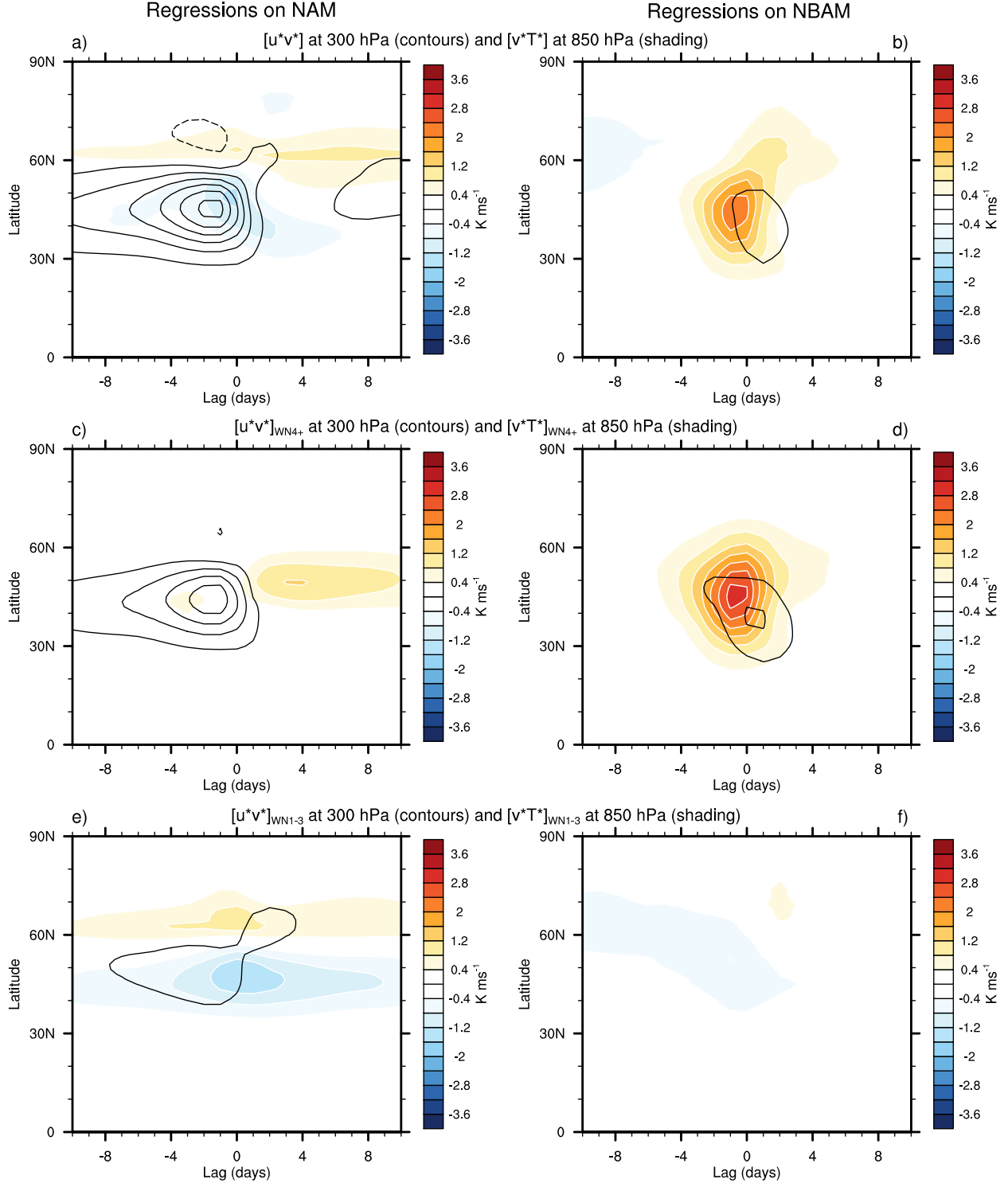


FIG. 4. Wavenumber breakdown of the latitude/lag structure of NAM and NBAM in the eddy fluxes of heat and momentum. Results show daily-mean, zonal-mean values of the fields indicated regressed on standardized values of the NAM (left) and NBAM (right) indices as a function of latitude and lag. (top) unfiltered data (reproduced from the corresponding results in Fig. 3). (middle and bottom) the components of the regressions in the top panels that are due to synoptic (zonal wavenumbers 4 and higher) and planetary scale (zonal wavenumbers 1–3) waves. Negative lags denote the field leads the base index, and vice versa. Contour interval is $4 \text{ m}^2 \text{ s}^{-2}$.

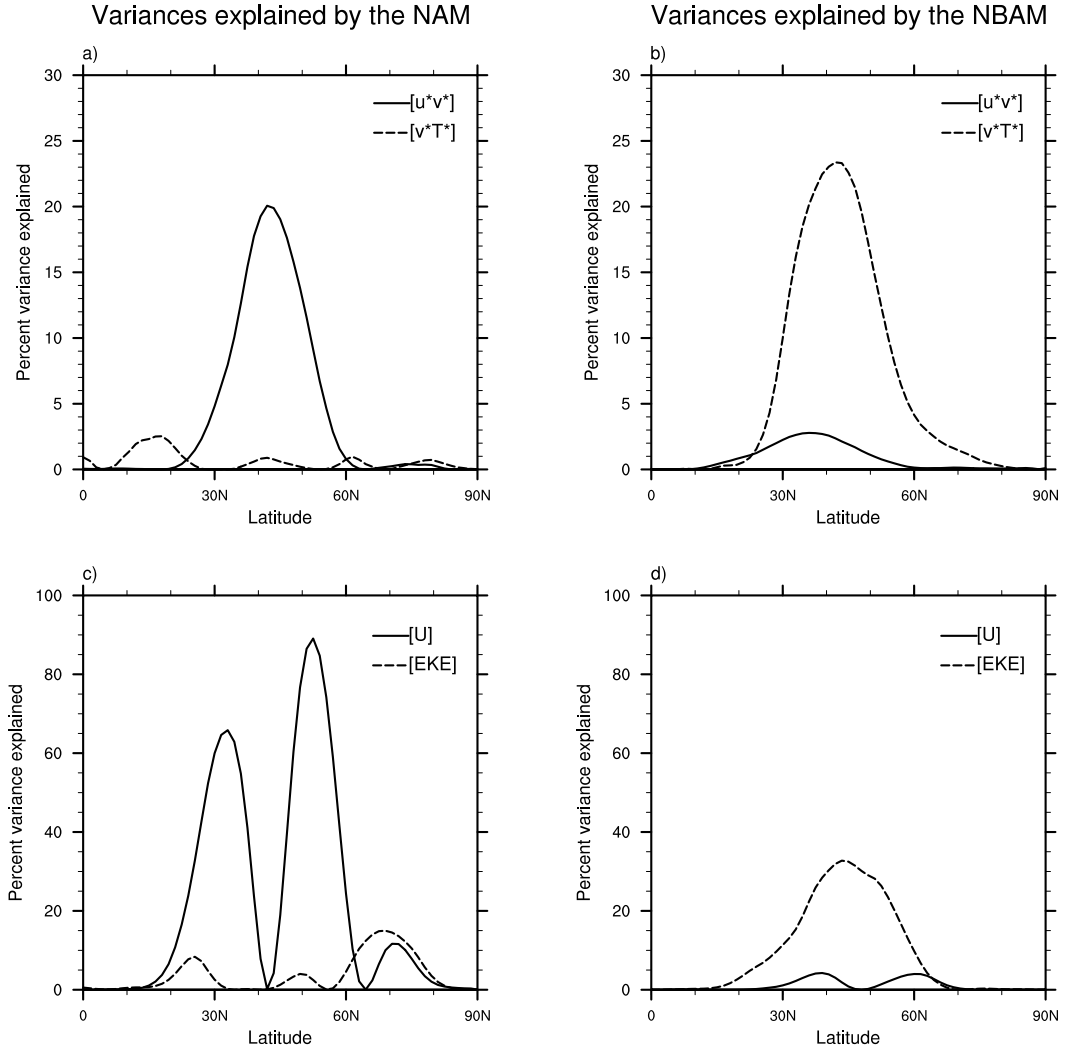
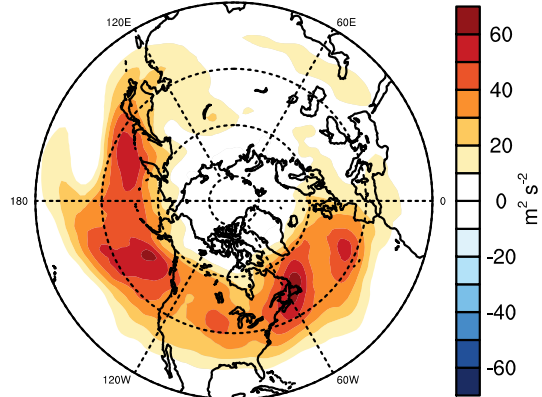


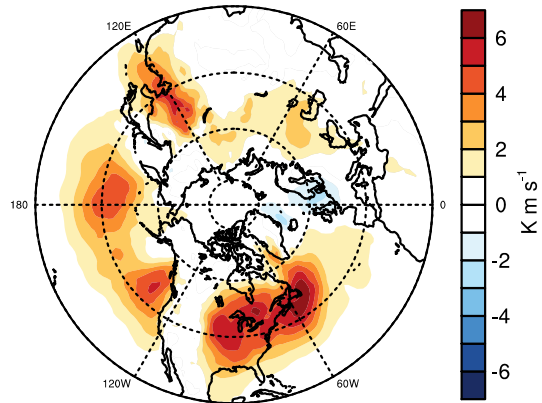
FIG. 5. Percent variance explained by the NAM (left) and NBAM (right) in vertically averaged values of the indicated fields. The time series and data are 10 day low-pass filtered to emphasize covariability on timescales longer than those associated with a typical baroclinic wave. The fields are vertically averaged between 950 and 250 hPa.

Regressions on NBAM

a) EKE at 300 hPa (lag 0)



b) $[v^*T^*]$ at 850 hPa (lag -1)



c) Precipitation (lag -1)

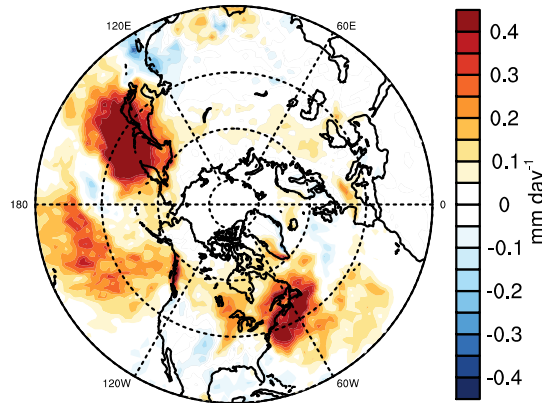


FIG. 6. Horizontal structure of the NBAM in EKE, the eddy fluxes of heat and precipitation. Results show daily-mean eddy kinetic energy at 300 hPa (top), the eddy fluxes of heat at 850 hPa (middle) and precipitation (bottom) regressed onto standardized values of NBAM index. The heat fluxes and precipitation lead the NBAM index by 1 day.

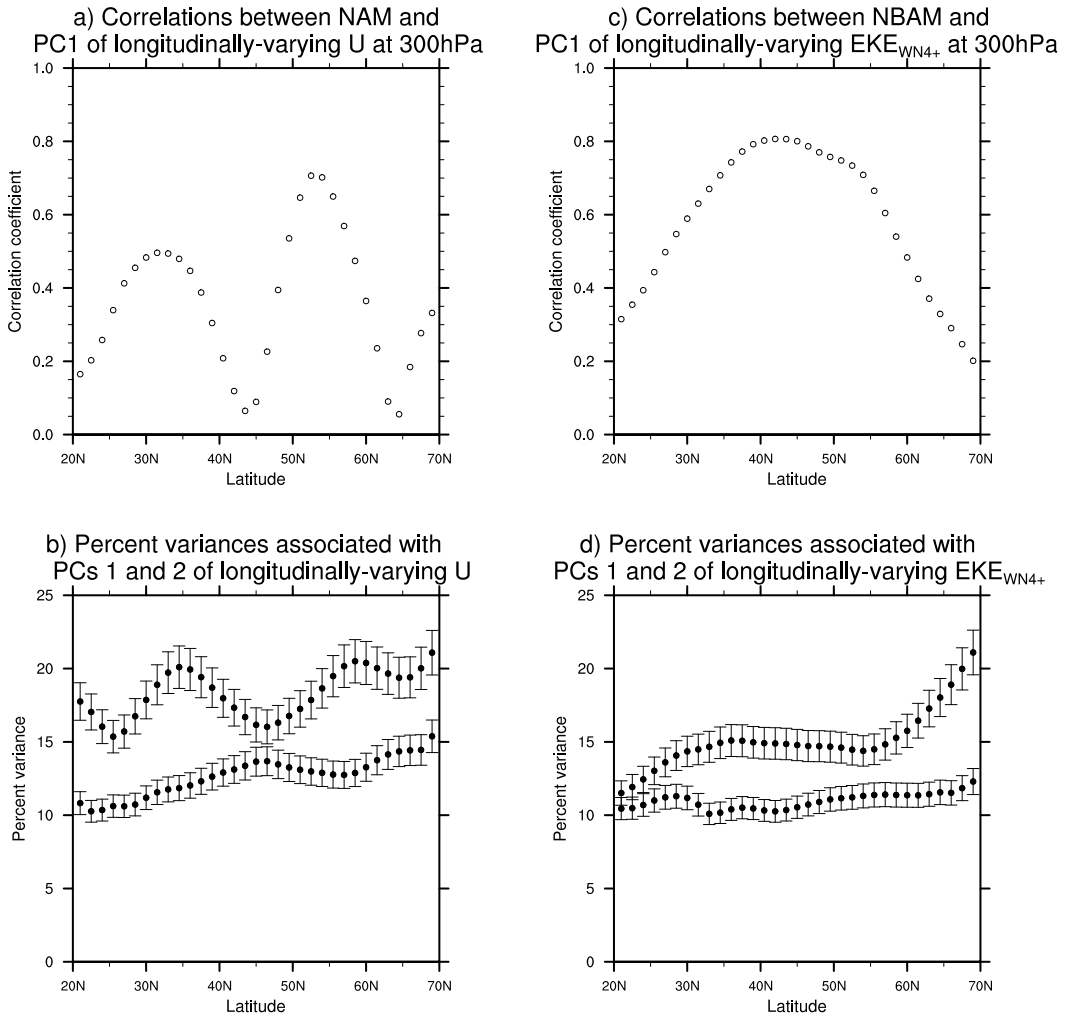


FIG. 7. (a) Correlations between the NAM index and the leading PCs of the daily-mean, longitudinally-varying zonal wind. The PCs are calculated as a function of latitude. (b) Variances explained by the first and second PCs of the daily-mean, longitudinally-varying zonal wind. (c) As in (a), but for correlations between the NBAM index and the leading PCs of daily-mean, synoptic-scale eddy kinetic energy. (d) As in (b), but for the PCs of the daily-mean, synoptic-scale eddy kinetic energy. Error bars are derived from the significance test described in North et al. (1982). The PCs are calculated based on daily-mean data. The correlations are based on 10 day low-pass versions of the time series to emphasize covariability on timescale longer than those associated with a typical baroclinic wave.

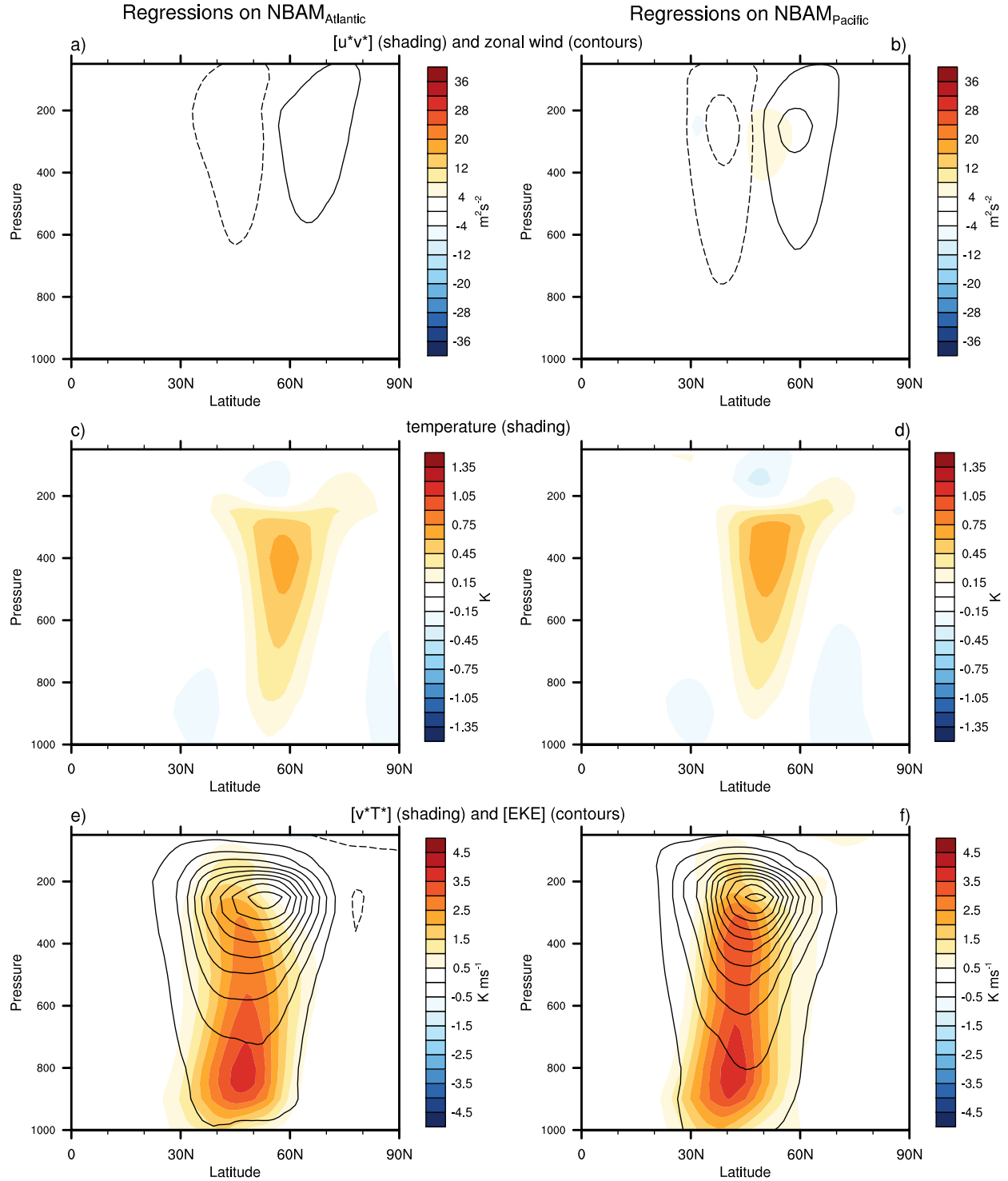


FIG. 8. Structure of baroclinic annular variability over the North Atlantic and North Pacific sectors of the hemisphere. As in the right column of Figure 2, but for results calculated separately for the Atlantic (left; 90°W–50°E) and Pacific (right; 110°E–110°W) sectors of the hemisphere. The NBAM_{Atlantic} is defined as the leading PC time series of synoptic-scale EKE in the Atlantic sector from 1000–200 hPa; the NBAM_{Pacific} index as the leading PC time series of synoptic-scale EKE in the Pacific sector from 1000–200 hPa.

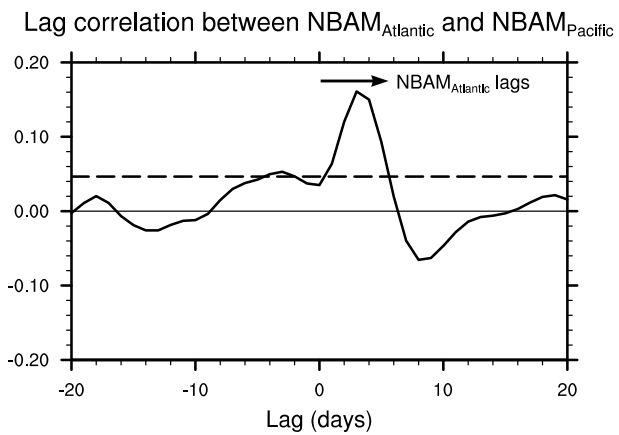


FIG. 9. Lead/lag correlations between the NBAM_{Pacific} index and NBAM_{Atlantic} index. Negative lags denote the NBAM_{Atlantic} index leading the NBAM_{Pacific}, and vice versa. The horizontal dashed line indicates the 99% significance level based on a two-tailed test of the *t*-statistic.

Regression of EKE at 300 hPa on NBAM_{Pacific}

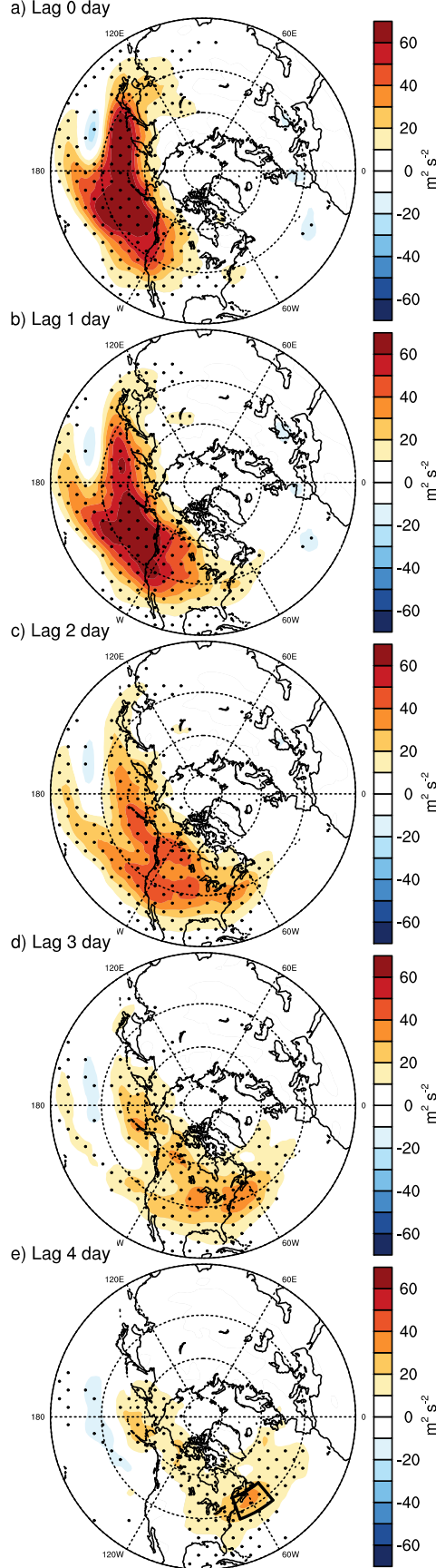


FIG. 10. Regressions of eddy kinetic energy at 300 hPa onto the NBAM_{Pacific} index as a function of lag. Stippling indicates results that exceed 99% confidence level based on a two-tailed test of the *t*-statistic.

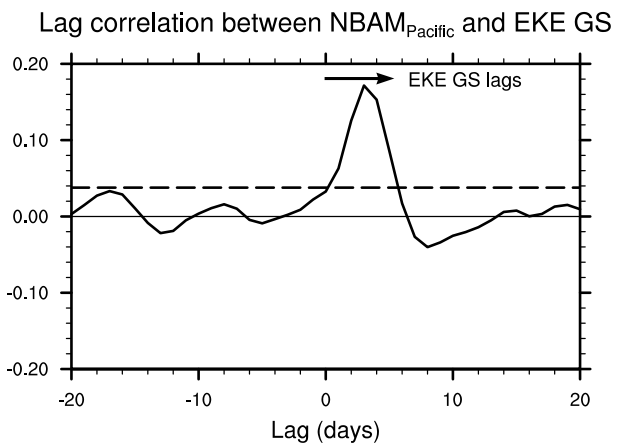


FIG. 11. As in Fig. 9, but for lead/lag correlations between the NBAM_{Pacific} index and eddy kinetic energy at 300 hPa averaged over Gulf Stream extension region (GS; see black borders indicated in Fig. 10e). Horizontal line indicates 99% significance levels based on a two-tailed test of the *t*-statistic.

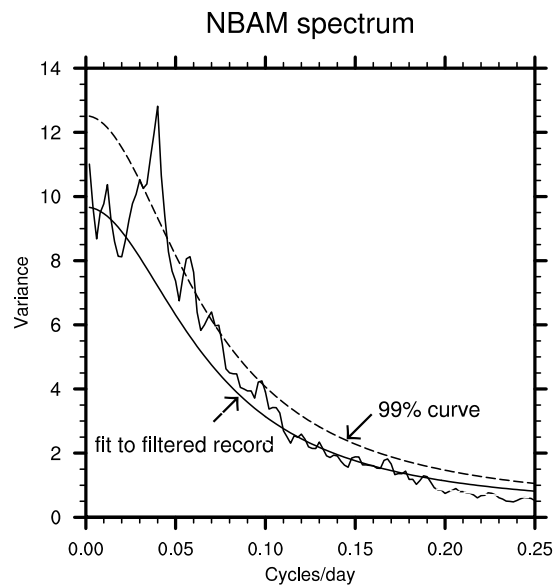


FIG. 12. Power spectra of the NBAM index calculated from daily-mean data for all calendar days. Solid and dashed lines indicate a) the red noise fit to the 20-day high pass filtered NBAM index and b) the 99% confidence level, respectively. See text and Appendix for details of the calculation.

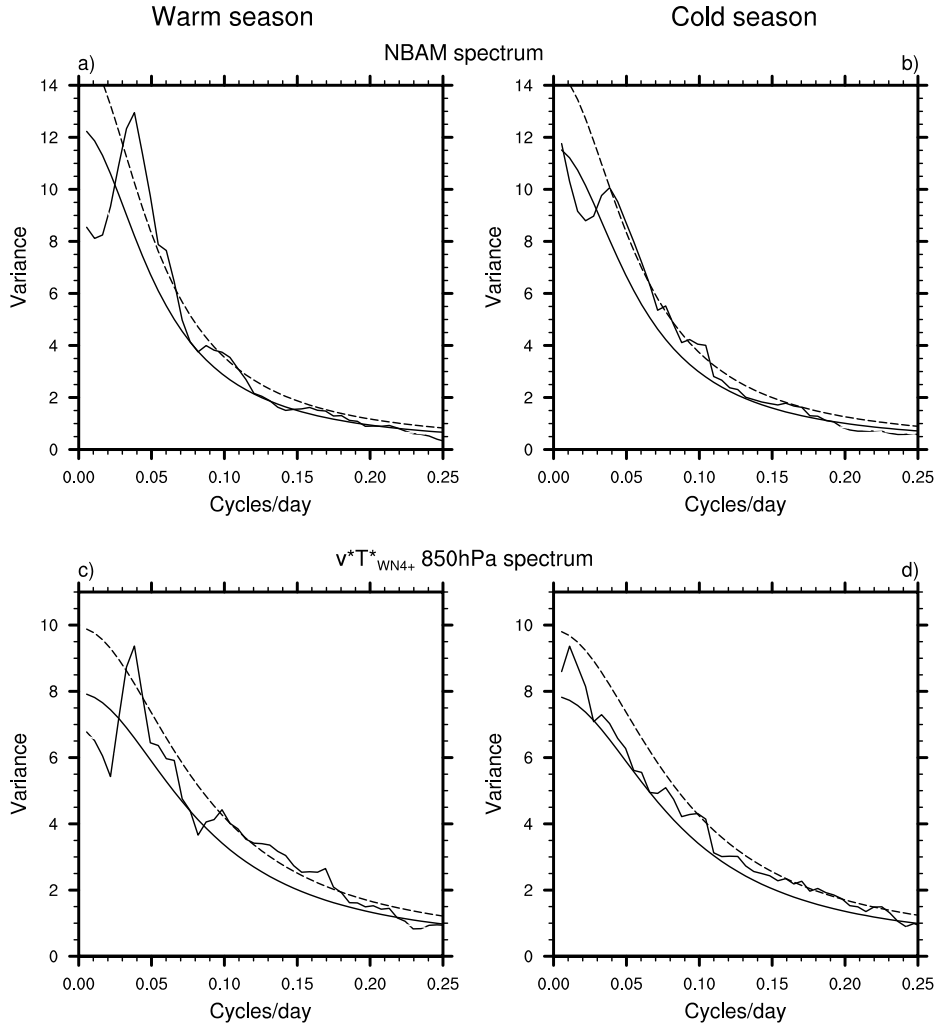


FIG. 13. Power spectra of the NBAM index (top), and the synoptic-scale eddy fluxes of heat at 850 hPa averaged 30° to 70° N (bottom). Results are calculated based on daily-mean data during the warm (left) and cold (right) seasons. Warm and cold seasons are defined as April–September, and October–March, respectively. Solid and dashed lines indicate a) the red noise fit to the 30-day high pass filtered time series and b) the 99% confidence levels, respectively. See text for details of the calculation. Note that the differences in spectral resolution between the results shown in Figs. 12 and 13 are due to the different subset lengths used in the calculations (Section 2).

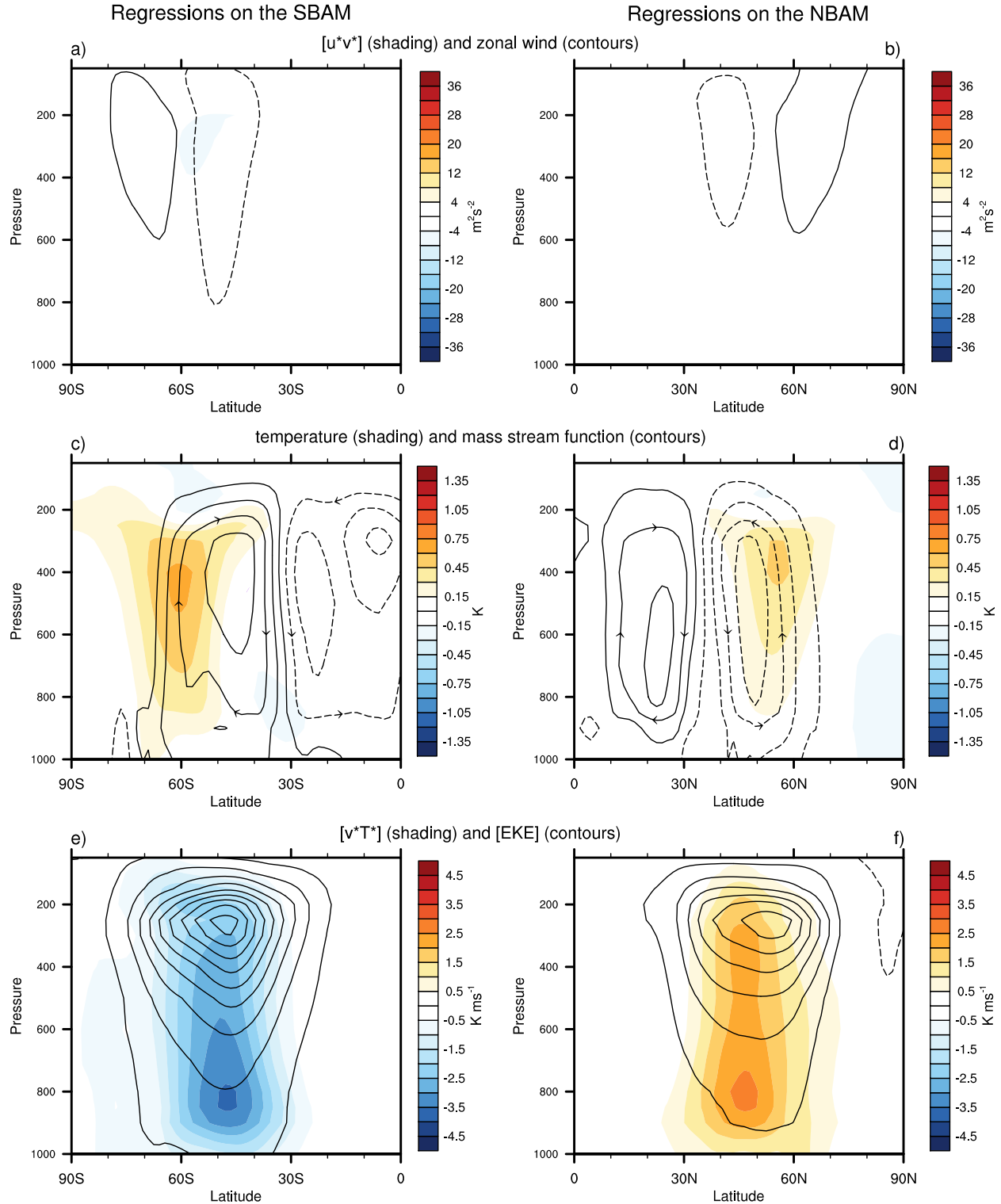


FIG. 14. Comparing the vertical structures of the southern and northern baroclinic annular modes. Results show daily-mean, zonal-mean values of the fields indicated regressed on standardized values of the SBAM (left) and NBAM (right) indices. Results for the NBAM are reproduced from Fig. 2 (right column). Results for the SBAM are reproduced from TW (but based on the period of record January 1979–December 2011).

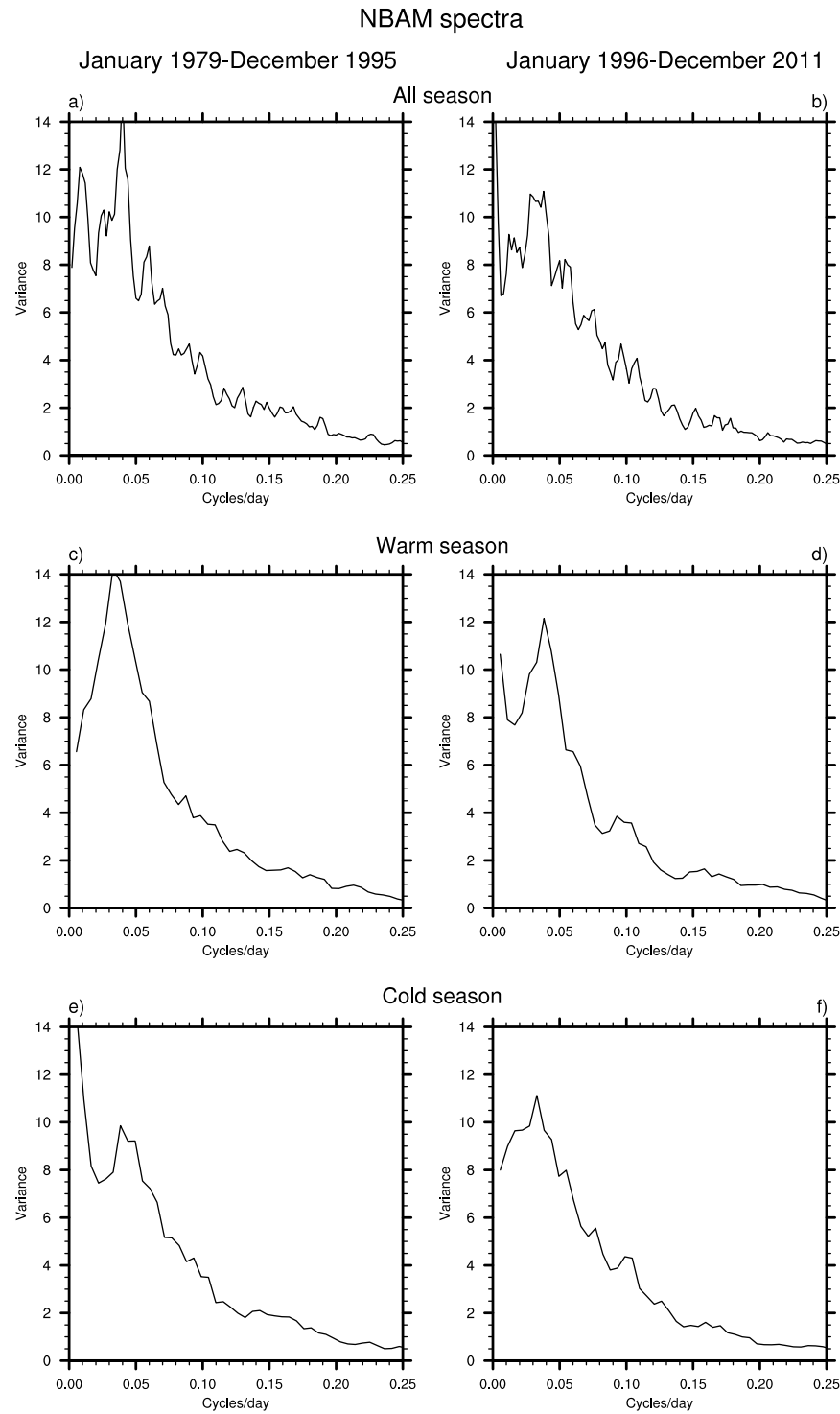


Figure A1: As in Figure 12b, but left panels show spectra of the NBAM for the first half of the data record, and right panels show spectra for the second half of the data record.

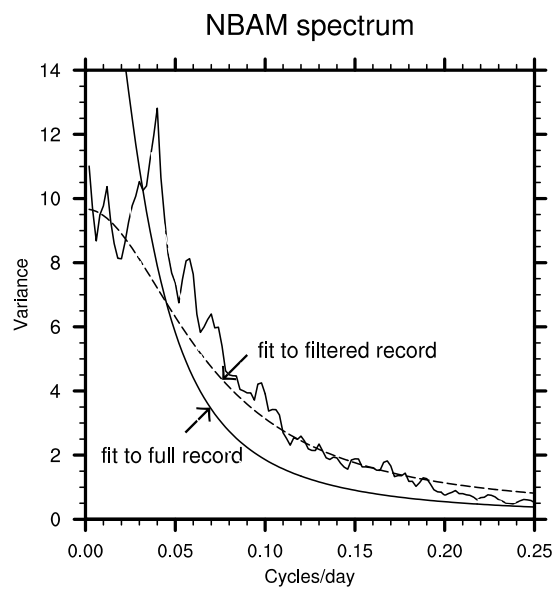


Figure A2: The power spectra of the NBAM index is reproduced from Fig. 12. Solid and dashed lines indicate the red noise fit to the a) unfilled NBAM index and b) 20-day high pass filtered NBAM index, respectively.